

Key Points:

- Wave modeling was used to test the hypothesis that 4 examples of lithified bedforms observed by the Curiosity rover are wave ripples
- 3-m-wavelength bedforms are thin-atmosphere aeolian ripples formed before the last subaqueous deposition ended in Gale crater
- Three examples remain viable candidates for wave ripples-which would indicate a lake that was largely free of ice at time of deposition

Correspondence to:

D. M. Rubin,
drubin@ucsc.edu











Citation:

Rubin, D. M., Lapôtre, M. A. G., Stevens, A. W., Lamb, M. P., Fedo, C. M., Grotzinger, J. P., et al. (2022). Ancient winds, waves, and atmosphere in Gale crater, Mars, inferred from sedimentary structures and wave modeling. *Journal of Geophysical Research: Planets*, 127, e2021JE007162. <https://doi.org/10.1029/2021JE007162>

Received 3 JAN 2022

Accepted 28 MAR 2022

Ancient Winds, Waves, and Atmosphere in Gale Crater, Mars, Inferred From Sedimentary Structures and Wave Modeling

D. M. Rubin¹ , M. A. G. Lapôtre² , A. W. Stevens³, M. P. Lamb⁴, C. M. Fedo⁵, J. P. Grotzinger⁴, S. Gupta⁶, K. M. Stack⁷ , A. R. Vasavada⁷ , S. G. Banham⁶ , A. B. Bryk⁸ , G. Caravaca⁹ , J. R. Christian¹⁰ , L. A. Edgar¹¹ , and M. C. Malin¹² 

¹Department of Earth & Planetary Sciences, UC Santa Cruz, Santa Cruz, CA, USA, ²Department of Geological Sciences, Stanford University, Stanford, CA, USA, ³US Geological Survey, Pacific Science Center, Santa Cruz, CA, USA, ⁴Division of Geological & Planetary Sciences, California Institute of Technology, Pasadena, CA, USA, ⁵Department of Earth & Planetary Sciences, UT Knoxville, Knoxville, TN, USA, ⁶Earth Science and Engineering, Imperial College, London, UK, ⁷Jet Propulsion Laboratory, Pasadena, CA, USA, ⁸Earth & Planetary Sciences, UC Berkeley, Berkeley, CA, USA, ⁹UMR 5277 IRAP, University Paul Sabatier Toulouse 3, Toulouse, France, ¹⁰Department of Earth and Planetary Sciences, McDonnell Center for the Space Sciences, Washington University in St. Louis, St. Louis, MO, USA, ¹¹USGS Astrogeology Science Center, Flagstaff, AZ, USA, ¹²Malin Space Science Systems, San Diego, CA, USA

Abstract Wave modeling and analysis of sedimentary structures were used to evaluate whether four examples of symmetrical, reversing, or straight-crested bedforms in Gale crater sandstones are preserved wave ripples; deposition by waves would demonstrate that the lake was not covered by ice at that time. Wave modeling indicates that regardless of atmospheric density, winds that exceeded the threshold of aeolian sand transport could have generated waves capable of producing nearshore wave ripples in most grain sizes of sand. Reversing 3-m-wavelength bedforms in the Kimberley formation are interpreted not as wave ripples but rather as large aeolian ripples that formed in an atmosphere approximately as thin as at present. These exhumed bedforms define many of the ridges at outcrops that appear striated in satellite images. At Kimberley these bedforms demonstrably underlie and therefore predate subaqueous beds, suggesting that a thin atmosphere existed at least temporarily before subaqueous deposition ceased in the crater. The other three candidate wave ripples (Square Top, Hunda, and Voe) are consistent with modeled waves, but other origins cannot be excluded. The predominance of flat-laminated (non-rippled) beds in the lacustrine Murray formation suggests that some aspect of the lake was not conducive to formation or preservation of recognizable wave ripples. Water depths may generally have been too deep, lakebed sediment may have been too fine-grained, the lake may have been smaller than modeled, or the lake may have been covered by ice.

Plain Language Summary Wave modeling and analysis of sedimentary structures were used to evaluate whether ancient lake deposits in Gale crater contain ripples formed by waves on the surface of the lake. Deposition by waves would show that the lake was not covered by ice at that time. Modeling shows that regardless of atmospheric density, winds capable of moving sand on land would generally have been strong enough to form waves that would produce ripples near shore. Large bedforms in the Kimberley formation are interpreted as ripples formed by the wind in an atmosphere similar to that of Mars today. These bedforms underlie and are older than other beds deposited in water, thereby showing that a thin atmosphere existed at least temporarily before deposition in water ceased in the crater. Three other candidate wave ripples are consistent with modeled waves, but other origins are possible. Thick sequences of sedimentary rock in Gale crater are flat-laminated rather than rippled, suggesting that some aspect of the lake was not favorable for their formation or preservation. Much of the lake may have been too deep or ice-covered, or the lake may have been smaller than modeled or had sediment too fine to form easily observed ripples.

1. Introduction

1.1. Purpose and Overview

Although lakes existed in Gale crater (Grotzinger et al., 2015), the question remains whether or not the lakes were free of ice. Lack of ice would indicate a warmer and denser atmosphere than on Mars today. One indicator of lack of ice cover would be ripples formed by wind-generated waves on the surface of the lake. Here we examine four

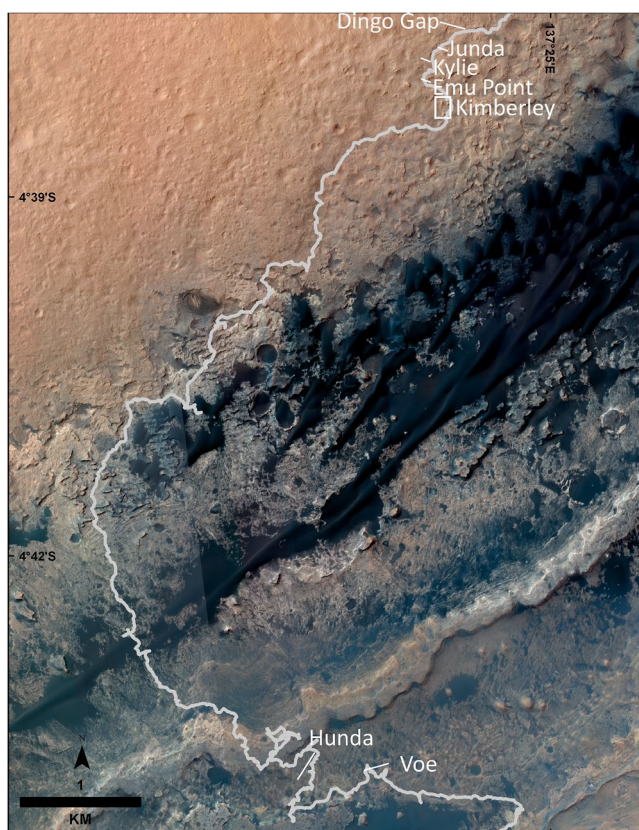


Figure 1. Traverse map of *Curiosity's* route showing locations of outcrops discussed in the text. The white rectangle at Kimberley shows the area in Figure 6a. Image Credit: NASA/JPL-Caltech/University of Arizona.

candidate wave ripples and use the SWAN wave model (Booij et al., 1999) to consider whether these sedimentary structures are consistent with the waves modeled for a lake in Gale crater.

1.2. Setting

The *Curiosity* Mars rover has traveled more than 25 km through Gale crater (Figure 1) and has ascended more than 500 m in elevation; this elevation gain is used (e.g., Stein et al., 2020) as a proxy for thickness of the stratigraphic sequence (Figure 2). Most of this route traversed sedimentary rocks that were deposited by rivers that flowed into the crater from the north rim (Williams et al., 2013) or that were deposited in a lake or a series of lakes, in the depression between the crater's north rim and its impact-formed central peak (Edgar et al., 2020; Grotzinger et al., 2015; Stack et al., 2019). During this traverse, *Curiosity* observed ancient deposits with morphology or stratification suggestive of formation by reversing flows. We use these distinctive structures to interpret ancient flow conditions.

1.3. Previous Work on Winds Along *Curiosity's* Traverse in Gale Crater

Modern winds along *Curiosity's* traverse on the north flank of Mt. Sharp in Gale crater typically blow upslope (toward the south or southeast) during the day and downslope (toward the north or northwest) at night (Baker et al., 2018; Newman et al., 2017). Dunes in this region are oriented ENE-WSW, and net sand transport (determined from motion of ripples and dunes in HiRISE satellite images) is oriented along the dune crests, toward the southwest quadrant (Baker et al., 2018; Bridges et al., 2017; Lapôtre & Rampe, 2018; Silvestro et al., 2013). Winds from north (from the crater rim) alternating with winds from the east or southeast could cause the observed sand transport and the observed orientation of the Bagnold dunes (dunes on a partially starved bed growing through the finger mode of Courrech du Pont et al., 2014).

Day and Kocurek (2016) examined a variety of geomorphic aeolian features in the vicinity of the rover traverse. These features were formed by recent winds as well as winds that persisted long enough to form structures on a geologic scale. They concluded that the dominant winds were regional winds from the north, with secondary katabatic winds flowing both south from the north rim and down Mt. Sharp, which is toward the north in the vicinity of the traverse. They interpreted dune slip faces that dip toward the NW as indicators of transport from the SE quadrant.

Directions of ancient winds in Gale crater can be inferred from observations of aeolian stratification in the Stimson formation, which was deposited on the flank of Mt. Sharp after the climate changed from wet to dry between 3.7 and 3.2 Gya. Aeolian stratification suggests that dunes had a similar orientation to modern dunes, but sand transport along the lengths of the dunes was to the northeast rather than southwest (Banham et al., 2018). Although the net sand-transport direction along the dune thus changed by approximately 180°, a modest rotation of one of the two directional wind modes is sufficient to reverse the resultant of the two opposing wind vectors (Courrech du Pont et al., 2014; Rubin & Hunter, 1987). For example, equal transport from 340° (NNW) and S (180°) would cause sand transport toward the NE quadrant, and a 60° rotation of the S wind to 120° would rotate the resultant direction to the SW quadrant.

Although the winds that formed the Stimson dunes are inferred to have fluctuated or reversed, the only reversals that have been detected have been on seasonal and longer time scales (Banham et al., 2021). Deposits of daily

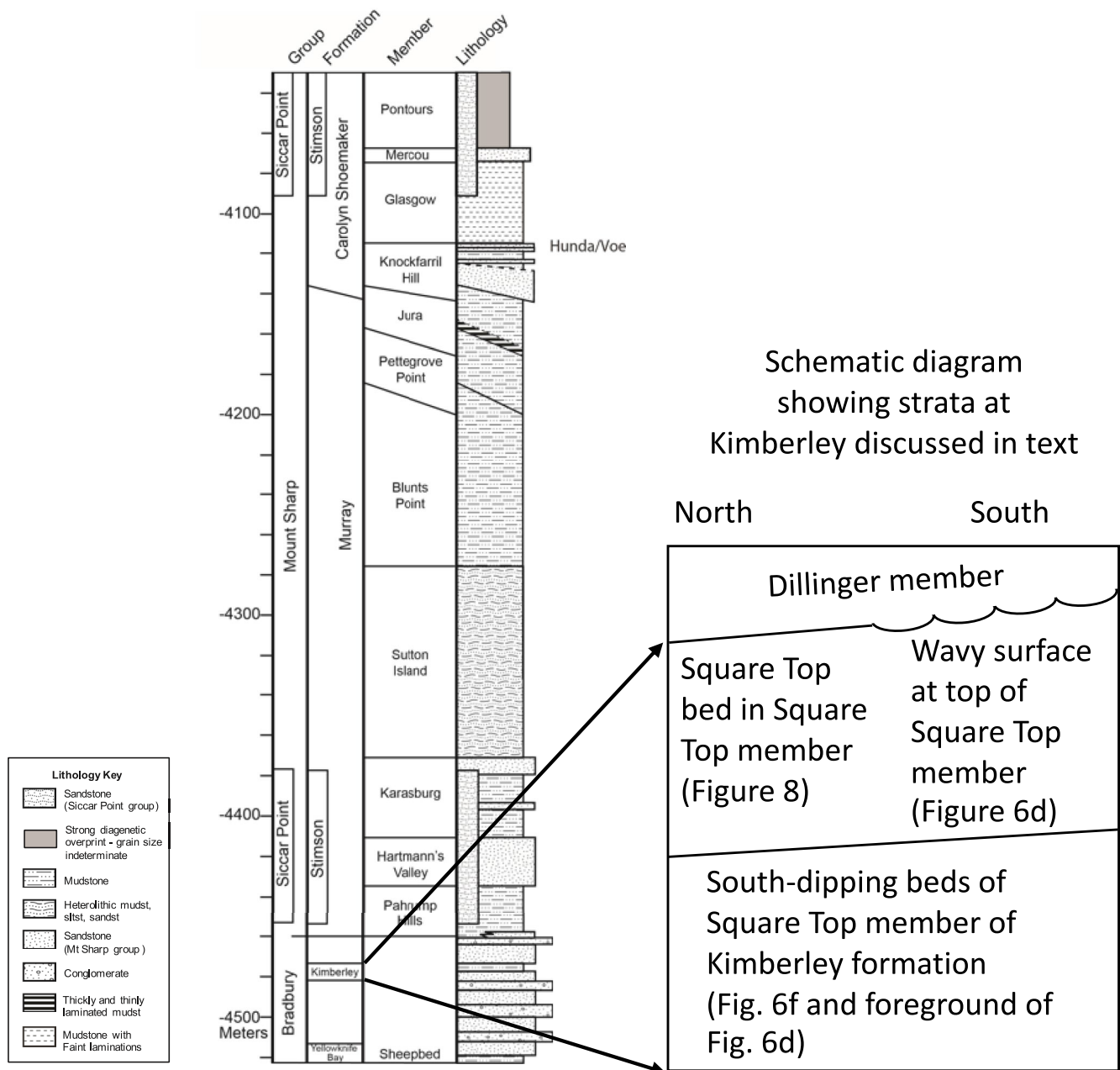


Figure 2. Stratigraphic section showing locations of sedimentary structures discussed in the text. The schematic diagram at the right shows the stratigraphic relations of structures at Kimberley discussed in the text and shown in Figures 6 and 8. See also Rice et al. (2017, Figure 5).

reversing winds have not been reported in the Stimson, perhaps because the dunes moved too small a distance to be detectable during individual day/night cycles.

The Shaler outcrop on the floor of Gale crater also contains aeolian beds (Edgar et al., 2017). These deposits demonstrate that winds were sufficient to transport sand, but the stratification does not provide details about directional properties of winds. Model results (Kite, Lewis, et al., 2013), however, suggest that Hesperian winds in Gale crater also reversed upslope-downslope from day to night. In summary, modern observations, ancient deposits, and model results indicate that winds blew with speeds exceeding the threshold for sand transport, with transport both to the north and south.

In summary, both modern and ancient winds in Gale crater transported aeolian sand toward a variety of directions. This observation is key to the wave modeling methods (Methods Sections 2.1 and 2.2) because it demonstrates that winds routinely exceeded the threshold of aeolian sand transport.

2. Methods

This study involves five kinds of methods: modeling waves generated by predicted winds in a lake in Gale crater; predicting wind speeds and atmospheric pressures for use in the wave model; predicting what ripples the modeled waves could have produced; processing of images taken by *Curiosity's* Mastcam; and interpretation of candidate wave ripples observed in those images. These five methods are discussed below.

2.1. Methods to Model Waves on a Lake in Gale Crater

To explore the possibility that winds that are strong enough to initiate aeolian transport of sand are also sufficient to generate sand-transporting waves on a lakebed, we followed the approach of Banfield et al. (2015) and used the SWAN wave model in Delft3D software (Booij et al., 1999). We modified and recompiled that open-source code (<https://oss.deltares.nl/web/delft3d/downloads>) to incorporate variable atmospheric density.

Banfield et al. tested their model results with experiments in a low-pressure wind tunnel (NASA Ames MARSWIT) and found that the model accurately described development of waves at low pressure. They then modeled a lake that filled Gale crater. In contrast, we specified a smaller and shallower lake, consistent with the paleogeography inferred by Grotzinger et al. (2015), although episodes of lake deposition likely occurred multiple times, with lakes varying in size. The modeled lake's north shore was at the Kimberley outcrop (Grotzinger et al., 2015) and its south shore on the north flank of the crater's inferred central peak. This modeled lake basin thus had a fetch of approximately 20 km (in a north-south direction). The modeled depth was 10 m (following Grotzinger et al., 2015, and Rice et al., 2017) that sloped up to the shoreline over a distance of 120 m. The model grid contained 50 grid cells along the length of the lake that were spaced at 1.2 km intervals from the upwind coastline to 18 km downwind. Between 18 km and the shoreline, the grid spacing gradually decreased to as fine as 6.5 m to better resolve shallow-water processes. Specifics of the computational grid, bathymetry, boundary conditions, and numerical and physical parameters used in the wave simulations are provided in Stevens and Rubin (2022). Wave development was simulated for 24 frequency bins between 0.05 and 1 Hz using 3rd generation physics and default values for bottom friction, white-capping, depth-induced breaking, and wind growth (Deltares, 2018).

2.2. Methods to Predict Wind Speeds and Atmospheric Pressures to Use in the Wave Model

The SWAN wave model requires that both wind speed and atmospheric density be specified, but we know neither of these values independently. The presence of wind-transported sands and sandstones in Gale crater, however, demonstrates that winds were strong enough to initiate aeolian transport of sand, and for any given atmospheric density we can calculate the wind speed needed to initiate that transport. Because the threshold wind shear velocity required to sustain saltation (impact threshold) is lower than the shear velocity threshold to initiate it (fluid threshold, u_{*f}) on Mars (e.g., Kok, 2010), ripple-maintaining winds often could have been weaker than the fluid threshold. Nevertheless, shear velocity of the winds must have at least occasionally exceeded u_{*f} in order to initiate saltation. To account for uncertainty related to the speed of past Martian winds, we make the conservative assumption that wind shear velocity at least occasionally equaled u_{*f} on land, and we explore scenarios using winds with shear velocities ranging from $\frac{1}{4}$ to 4 times u_{*f} .

We use the formulation of Andreotti et al. (2021) to estimate the value of u_{*f} for a basaltic ($\rho_s = 2,900 \text{ kg/m}^3$) 125- μm grain under three different atmospheric pressures ($p = 6, 60, 600 \text{ mbar}$) on Mars ($g = 3.71 \text{ m/s}^2$). We assume an atmospheric molar mass of 44.01 g/mol (pure CO_2), and a surface temperature of 273 K because water needs to be liquid for wave ripples to form, although results are found to be relatively insensitive to temperature. Because land and water bodies have different surface roughnesses, which affect wind shear velocities, we calculated the wind speed at a 10-m height above the bed (u_{10}) corresponding to our assumed wind shear velocity on land, and used the latter as the input wind speed at 10 m above the water surface for input in the SWAN wave model. The conversion from wind shear velocity (u_{*f}) to wind speed ($U(z)$) at a height z above the bed was performed using the law of the wall,

$$U(z) = \frac{u_{sf}}{\kappa} \ln \left(\frac{z}{z_0} \right),$$

where $\kappa = 0.41$ is the von Kármán constant and z_0 is a length scale that requires knowledge of the flow's aerodynamic roughness. Because we are considering conditions that initiate motion of sand, we follow Andreotti et al. (2021) and ignore the effect that a well-developed saltation cloud can have on aerodynamic roughness. We calculated a roughness Reynolds number as $Re_{k_s} = \frac{u_{sf} k_s}{\nu}$, where $k_s \approx 3d$ is a typical bed-roughness height with d the grain size, and ν is the kinematic viscosity of the atmosphere. We assumed an atmospheric dynamic viscosity of 1.4×10^{-5} Pa.s (pure CO₂). For $p = 6$ and 60 mbar, $Re_{k_s} < 4$, such that winds are expected to be aerodynamically smooth. In that case, z_0 is controlled by the presence of a viscous sublayer; we used $z_0 = \frac{\nu}{9u_{sf}}$. For $p = 600$ mbar, winds are expected to be in a transitional aerodynamic regime between smooth and rough conditions. In that case, z_0 does not differ much from that in the rough regime (Nikuradse, 1933), so we assumed $z_0 = \frac{k_s}{30} = \frac{d}{10}$. For $p = 6, 60$, and 600 mbar, we estimated $u_{10} = U(z = 10) = 30.0, 14.7$, and 4.3 m/s, respectively. The SWAN model uses an empirical relation to convert u_{10} to a boundary stress, and we assume that the relation is valid for Mars.

2.3. Methods to Predict Ripples From the Modeled Waves

To predict morphology of ripples produced by the modeled waves required three steps. First, we determined the paired values of modeled wave period and wave height along the cross-shore transects; depth along each transect ranged from 10 m for most of the lake, and then beginning at 120 m from the northern shore depth shallowed to zero, as shown in the top row in Figure 3. The second step was to search for the maximum wave period and wave maximum wave orbital velocity along each transect (Figure 4) for the three atmospheric pressures and five wind speeds (defined relative to the threshold for aeolian transport of sand). Finally, we followed the methods in Lamb et al. (2012) to calculate wavelengths and shapes of orbital ripples. An orbital ripples, which we do not model, would, for the same bedform wavelength, be generated under larger waves (Wiberg & Harris, 1994). Thus, our wave reconstructions can be taken as conservative.

For our calculations of ripple wavelengths and morphologies, we allowed the near-bed wave orbital velocity, U_{orb} , and the wave period, T , to vary across a wide range: $0.1 < U_{orb} < 2$ m/s and $1 < T < 20$ s. For each combination of wave period and orbital velocity along the transects, we calculated the near-bed orbital diameter, d_0 , from Airy wave theory, $d_0 = U_{orb} T / \pi$, and calculated the wave ripple wavelength by assuming that wavelength is 65% of near-bed orbital diameter (e.g., Pedocchi & Garcia, 2009). Next, using a numerical iteration scheme, we calculated the grain diameter, D , that is predicted to be at the threshold of stability for different bed states. We set the submerged specific density of sediment, $R = 2.0$, the acceleration due to gravity to 3.711 m/s², and the fluid kinematic viscosity to 10^{-6} m²/s. For the threshold of sediment motion at the onset of trochoidal ripples, we used the criterion of You and Yin (2006). For rounded ripples (or hummocks), we used $U_{orb} = 25w_s$ (Pedocchi & Garcia), in which w_s (grain settling velocity) was calculated from Dietrich (1982) using parameters for spheres. For plane bed, we followed the Lamb et al. (2012) analysis of data from Cummings et al. (2009) and Dumas et al. (2005) and used $u_*^2 / (RgD) = 3$. The bed shear velocity, u_* , was calculated from Grant and Madsen (1982) using an iterative scheme where the near-bed roughness was assumed to be $k_s = 2.5D$. This sequence of calculations yields ripple wavelength and morphology as a function of relative wind speed at each modeled location along the transects (Figure 5).

2.4. Images and Processing Methods

All images from the rover were taken using its Mastcam camera (Malin, 2013; Malin et al., 2017). Image numbers and subsequent processing of the Mastcam images are detailed in Table 1. Measurements of bedform wavelengths were made using JPL's MSLICE software. A public measurement tool is available at NASA Planetary Data Systems, (MSL Analyst's Notebook, Stein et al., 2016). All satellite images were taken with the Mars Reconnaissance Orbiter's HiRISE High Resolution Imaging Science Experiment (McEwen, 2007).

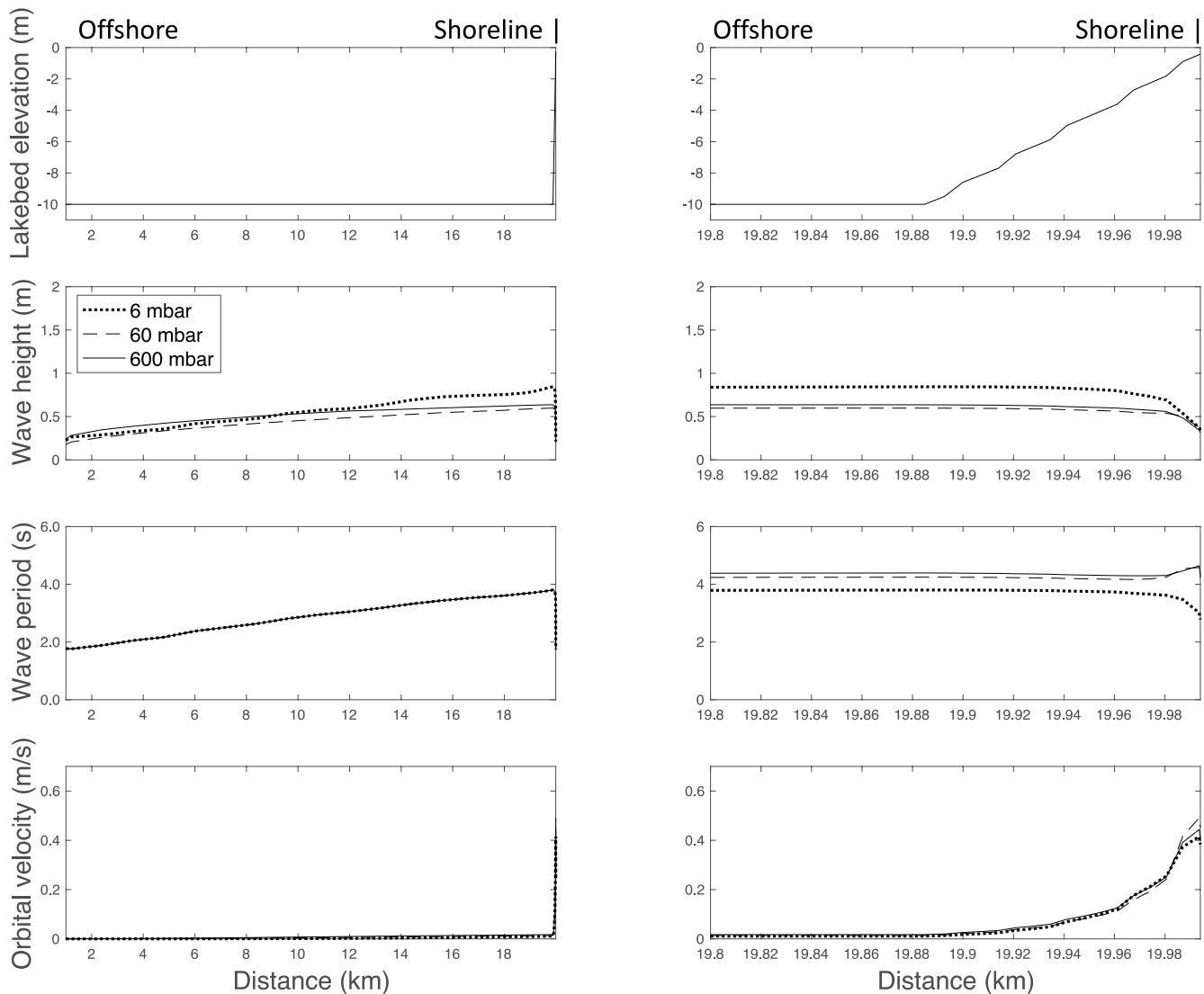


Figure 3. Wave-model results showing offshore-onshore transects of lakebed elevation, wave height, wave period, and orbital velocity, for winds at the threshold of aeolian sand transport in three atmospheric densities. Distance is measured from the south shore of a 20-km wide lake; 20-km location is the north shore of the lake (at Kimberley). The left column of four plots shows results for the full transect; the right column shows the 200 m nearest to shore. Lake depth is 10 m until 120 m from shore. Wave height and period increase with distance as waves undergo forcing by winds. Wave orbital velocity increases substantially in the 100 m closest to shore, where the lake shallows and waves interact with the bed. Threshold wind speeds are 30.0, 14.7, and 4.3 m/s in atmospheric densities of 6, 60, and 600 mbar, respectively. Changing the atmospheric density by a factor of 100 causes relatively minor changes in waves.

2.5. Methods for Identifying and Interpreting Deposits of Reversing Bedforms

Bedforms in reversing flows have three idealized characteristics: long straight parallel crests (Tanner, 1967; Rubin, 2012, Figure 1), relatively symmetrical across-crest profiles, and stratification that records reversing migration, such as interleaved zigzagging cross-laminae at the crests. Examples of such structures are shown by Rubin and Carter (2006a, Figures 18–20), and animations showing formation of these structures are shown by Rubin and Carter (2006b, Figures 18–20 and Figures 19–20morph). These characteristics, however, are neither necessary nor sufficient to demonstrate formation by waves. One or more of these characteristics can originate in other settings: reversing winds; reversing subaqueous currents generated by tides or fluctuating eddy-reattachment zones in rivers (Rubin et al., 1990, Figure 8; Rubin & MacDonald, 1995; Rubin & Carter, Figures 7, 20, 64); and in density currents, including those in glacial lakes (Jopling & Walker, 1968). Moreover, wave ripples need not have any of these three characteristics. High orbital velocities or interfering waves can make wave ripples three-dimensional rather than straight-crested, and flows that are not perfectly symmetrical—either because of a

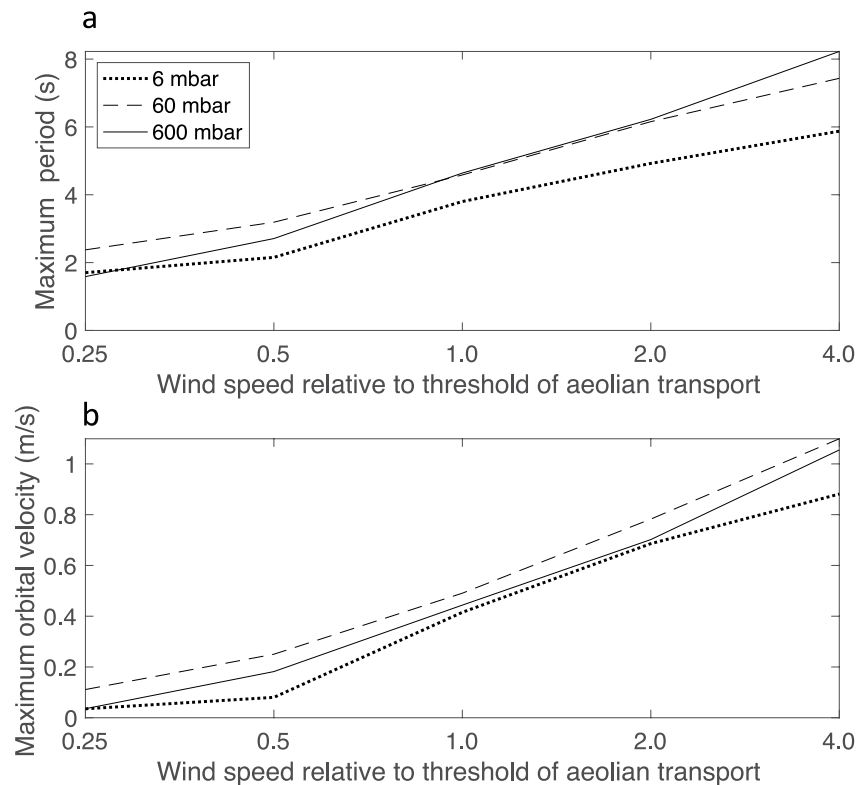


Figure 4. Upper and lower limits of (a) maximum orbital velocity and (b) maximum wave period along transects for five wind speeds (1/4, 1/2, 1, 2, and 4 times the threshold of aeolian transport) and three atmospheric densities.

superimposed current or because the wave-generated flows are affected by friction at the bed—can produce wave ripples that are asymmetrical and migrate in a preferred direction. Nevertheless, these three characteristics remain the best hints that waves may have affected a bed.

3. Results and Observations

In this section we first consider results and observations of winds sufficient to cause aeolian transport, then results of the wave and ripple modeling, and finally we consider four candidate wave ripples observed by *Curiosity*.

3.1. Wind Speeds Inferred From Aeolian Transport and Winds Measured by *Curiosity*

Evaluating whether or not the threshold wind speeds at an elevation of 10 m above the bed (u_{10}) are consistent with *Curiosity*'s measured winds is more complicated than merely comparing predicted and observed wind speeds. First, *Curiosity* measured winds at an elevation of 1.5 m above the bed rather than the 10-m elevation used for the predictions above; winds of 30 m/s at 10 m above the bed at 6 mbar correspond to a speed of slightly less than 25 m/s at an elevation of 1.5 m. Second, *Curiosity*'s wind instrument failed before the windy-season study of sand movement in the Bagnold dunes, so only weak-season winds were reported by Newman et al. (2017, Figures 11–13). Third, during the weak-wind season, the wind distribution exhibited a long tail with winds (at $z = 1.5$ m) that attained 20 m/s (Newman et al., 2017, Figures 11–13). Newman et al. (2017) did not report distributions of winds that exceeded 20 m/s, however, because of “increased uncertainty above this speed in the present retrieval algorithm”. Nevertheless, winds of 20 m/s (at $z = 1.5$ m) did occur during the low-wind season (i.e., when aeolian activity was not observed from orbit or from the ground); this was confirmed by Bridges et al. (2017). More recent analysis of *Curiosity*'s wind data (Viúdez-Moreiras et al., 2019, Figures 9 and 10) found that winds exceeded 20 m/s (at $z = 1.5$ m) between 0.5% and 1.5% of the time during midday and afternoon hours during the peak days of the windy seasons. Viúdez-Moreiras et al. (2019, Figure 2), also reported a tail in the distribution of wind speeds, up to a maximum of 25 m/s. This speed corresponds to the value of 30 m/s (at $z = 10$ m), the

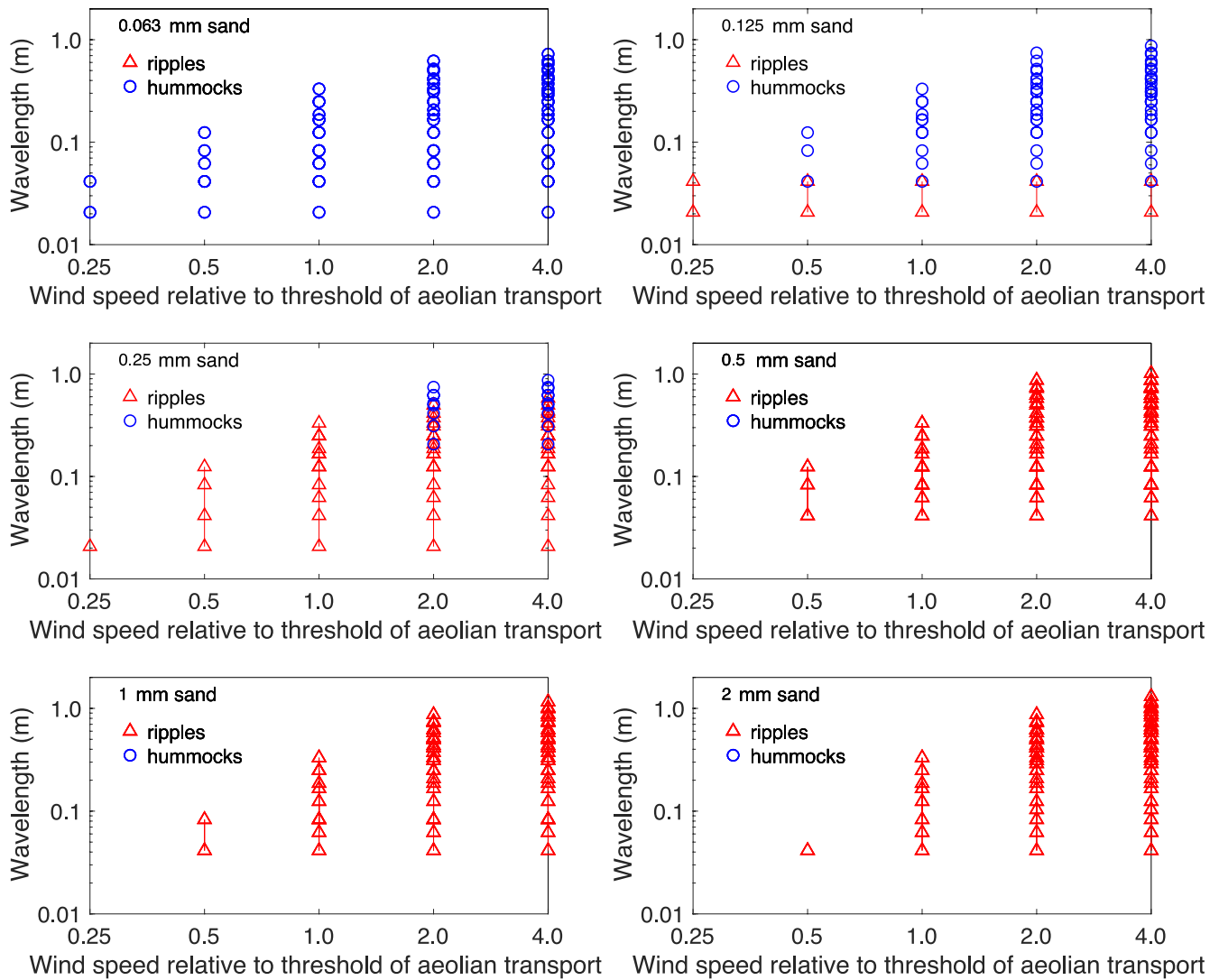


Figure 5. Predicted wavelength of ripples and hummocks in sand of six grain sizes in a 60 mbar atm. The finest sands make hummocks, and the coarsest make ripples. At intermediate grain sizes, hummocks form at higher orbital velocities than ripples.

elevation which we use for input in the SWAN wave model. The winds used to drive the wave modeling are thus consistent with the winds measured by *Curiosity* during windy midday and afternoon hours during windy times of the year.

3.2. Results of Wave Modeling

3.2.1. Modeled Waves in Atmospheres of Different Densities

We suspected that winds at the threshold of aeolian sand transport impose equal stress on the bed and therefore might produce similar waves. In fact, the modeled wave periods and orbital velocities for threshold winds at different atmospheric pressures are remarkably similar (Figures 3 and 4), but not identical. Allowing the modeled atmospheric density to vary by two orders of magnitude changes the threshold wind speeds for aeolian transport by almost an order of magnitude, but the modeled wave period and orbital velocities change by only $\pm 10\%$ (Figure 4). In a 6-mbar atmosphere, waves formed by winds at the threshold of aeolian transport have a slightly shorter period and slightly larger height than in a 600-mbar atmosphere, but the resulting orbital velocities are so similar that the values generally fall within the width of the lines plotted in Figure 4 for all but the 10 m nearest to

Table 1
Images and Processing

Figure 1d	Camera	Picture number	Processing
Figure 6a	HiRISE	ESP_018854_1755 ESP_018920_1755 ESP_058361_1755	Extras/MRGB color
Figure 6b	Mcam	sol595MRU002509	mosaic_proc.png
Figure 6c	HiRISE	ESP_018854_1755 ESP_018920_1755 ESP_058361_1755	Extras/MRGB color
Figure 6e	Mcam	sol0590MR002484	mosaic_proc.png
Figure 6f	Mcam	sol0580MR002407	mosaic_proc.png
Figures 7a,7b	Mcam	sol0538MR002121	mosaic_proc.png
Figure 7d	Mcam	sol0554MR002246	mosaic_proc.png
Figure 8	Mcam	sol0584MR002444	mosaic_proc.png
Figures 9a, 9b	Mcam	sol2575MR013526	mosaic_proc.png
Figure 9c	Mcam	sol2572MR013507	mosaic_proc.png
Figures 10a, 10c, and 10d	Mcam	sol2935ML015306	mosaic_proc.png
Figure 10b	Mcam	sol2936MR015316	mosaic_proc.png

Note. Mosaic_proc processing = expansion from 8-to-16-bit per channel, dark-correction, flat-field, field flattening, bad pixel repair, bayer-color array interpolation (de-mosaicing), green channel compensation, mosaicing in site frame and spherical coordinates with seam blending, white-balance color compensation, gray compensation, all in 16-bit per color channel. Finally linear conversion to 8-bit per channel (24-bit color).

the shoreline. For weaker winds (one-half or one-quarter of the threshold speed for sand transport), atmospheric density produces a larger difference in wave properties (Figure 4).

3.2.2. Modeled Waves and Ripples Along Each Transect, at Different Wind Speeds

Modeled wave height, wave period, and orbital velocity gradually increase downwind as winds continue to make waves grow larger, and wave height and orbital velocity increase substantially as waves enter shallower water within tens of meters of the shoreline (Figure 3). Ripple wavelength increases as the wind speed increases for a given atmospheric density (Figure 5). Wave ripples produced by winds that are only one quarter of the threshold for aeolian transport do not exceed a few cm, whereas winds that exceed 4 times the threshold wind speed are predicted to produce wave ripples with wavelengths that exceed 1 m (Figure 5). Ripple morphology and wavelength also depend on grain size, with finer sand producing smaller ripples with a more rounded, hummocky shape for a given orbital velocity.

Regardless of which paired values of wind speed and atmospheric density are used, any modeled winds that exceed the threshold of aeolian sand transport (and that are blowing in an onshore direction on a 10-m-deep ice-free lake) are sufficient to generate waves capable of producing wave ripples near shore (Figure 5). Even winds with speeds of only half the threshold for aeolian transport are capable of producing wave ripples in all grain sizes finer than 2 mm.

3.3. Observations and Interpretations of Deposits of Reversing Bedforms in Gale Crater

The following discussion considers four structures observed by *Curiosity* in rock outcrops in Gale crater that have one or more of these three characteristics. One example is interpreted to be large aeolian ripples. The other three structures are consistent with deposition by waves, but other alternatives cannot be definitively excluded.

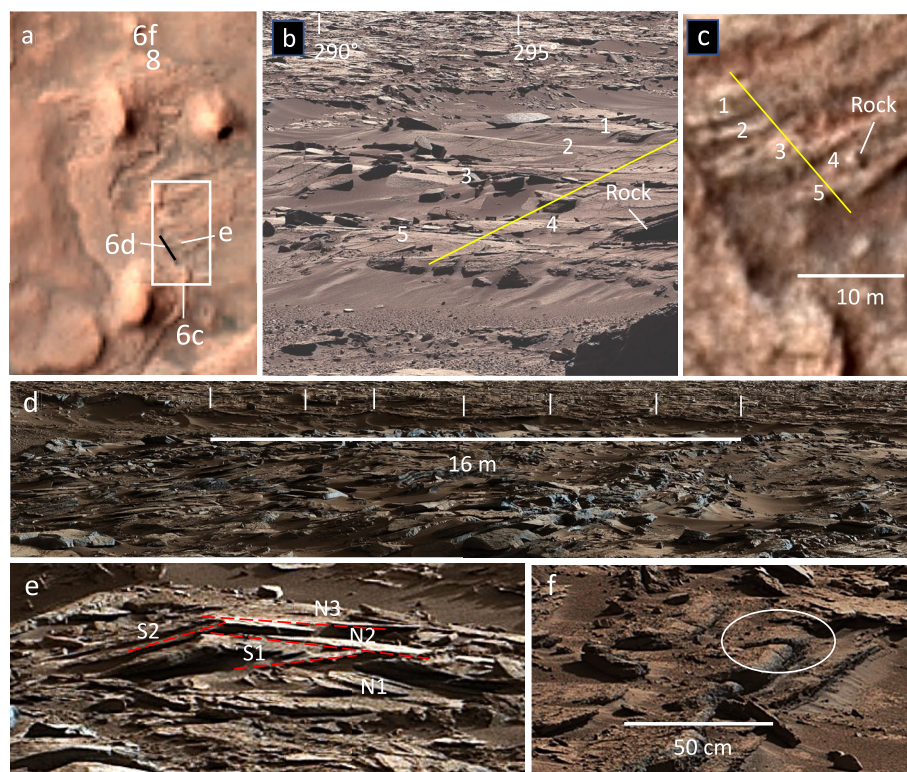


Figure 6. Morphology and sedimentology of striations, reversing bedforms, and overlying and underlying beds at Kimberley. Image Credit for a and (c) NASA/JPL-Caltech/University of Arizona. Image Credit for b, d-f: NASA/Caltech-JPL/MSSS. (a) Orbital view showing striated outcrop morphology. The white rectangle shows the location of the HiRISE image in (c). The white rectangle shows the region in Figure 6c. The black line indicates the location of the wavy bedforms in Figure 6. Other annotations show the locations of Figures 6e and 6f and 8. (b) Bedforms at Kimberley viewed toward the NNW by the rover's Mastcam camera. The bedforms are visible as striations in the HiRISE image (c). Five bedform crests (four wavelengths) span a distance of ~12 m, corresponding to a wavelength of 3 m. Sol 595, MR02509. (c) HiRISE image of area in the white rectangle in (a). (d) Wavy bed in Dillinger member. Seven crests, indicated by white lines, bracket six wavelengths over a distance of 16 m. Mean wavelength is 2.7 m; mean height is 10–20 cm. Sol 590 MR02484. (e) Internal stratification of a bedform showing north-south (N–S) reversals. Red dashed lines indicate bounding surfaces that separate north- and south-dipping sets of beds that are arranged in zigzags (Rubin and Hunter, 1983). Two complete reversal-cycles are preserved. The bedform in this image appears in Heydari et al. (2020, Figure 4c). Sol 590 MR02484. (f) Eroded upper surface of south-dipping beds of the Square Top member of the Kimberley formation (in white ellipse). This bed was cohesive enough to support nearly a nearly vertical slope when eroded. Sol 580 MR2407.

3.3.1. Three-m-Wavelength Reversing Bedforms in “Orbital Striated Outcrops” (OSOs)

3.3.1.1. Observations

For a distance of approximately 1.5 km, *Curiosity* traversed a belt of discontinuous outcrops that display ENE-WSW ridges in satellite images, including Dingo Gap, Junda, Kylie, Emu Point, and Kimberley (Figures 1, 6 and 7). Grotzinger et al. (2015) called these outcrops “orbital striated outcrops” or OSOs. Some of these outcrops are locally draped with ancient sediment bedforms that provide information about the flows that formed the bedforms and may have eroded the outcrops. The OSOs contain south-dipping strata that have been interpreted as foresets of small delta clinoforms deposited by rivers flowing south into a lake (Grotzinger et al., 2015; Le Deit et al., 2016; Rice et al., 2017) or the flanks of antidunes migrating south (upstream) in floods flowing down (northward) from Mt. Sharp (Heydari et al., 2020). All of these previous studies and that of Stack et al. (2016) have concluded that the orbital striations are formed by outcropping south-dipping strata. Although some OSOs are such outcropping south-dipping beds, other fields of striations are trains of preserved reversing bedforms (Figure 6). This alternative can be demonstrated by comparing images of the same outcrops viewed by both *Curiosity*'s Mastcam and HiRISE satellite. For example, the Kimberley outcrop includes bedforms with

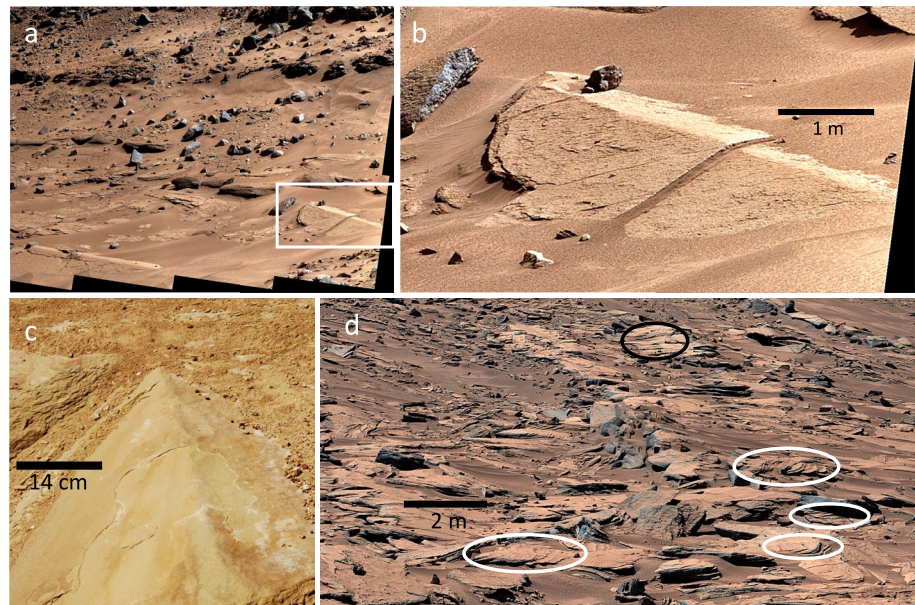


Figure 7. Bedform ridges at locations other than Kimberley. Mars images: NASA/Caltech-JPL/MSSS. (a) Mastcam image of an isolated bedform crest at Dingo Gap. White rectangle shows area enlarged in (b) Sol 538 MR02121. (b) Enlargement of area in white rectangle in (a) (c) Photograph of a preserved aeolian dune ridge in the Entrada Sandstone showing similar surface appearance to the bedforms in (b) Devil's Garden, southwest of Escalante, Utah. (d) South-dipping beds at Kylie draped with patchy veneer of north-dipping sediment (black ellipses) and discontinuous lenses of north-dipping cross-beds (white ellipses). View is toward the east. Sol 0554 MR02246.

distinctive features (bifurcations and a large rock) that can be correlated between Mastcam (Figure 6b) and HiRISE (Figure 6c) images.

The extent of sediment cover that mantles the south-dipping beds varies from outcrop to outcrop, forming a spectrum that ranges from bare truncated south-dipping beds (Junda, most of Kylie, and parts of Kimberley) to regions where the sand cover is sufficiently thick and widespread that preserved bedforms cover the surface almost completely, with little or no evidence of underlying strata (Kimberley, Figures 6b and 6c). At areas with intermediate sand cover (Kylie, Figure 7d), ridges of truncated south-dipping beds are locally draped on both north- and south-facing sides with thin veneers of sediment. (Another such partial drape is shown by Heydari et al., 2020, Figure 4c). At other locations, complete bedforms are exposed individually rather than in a train (Dingo Gap, Figures 7a and 7b), or their remnants occur in decimeter-thick discontinuous lenses of north- and south-dipping cross-beds that record reversing migration of bedforms that were not preserved intact (Kylie, white ellipses in Figure 7d, and Dingo Gap) due to subsequent erosion.

The bedforms are best displayed at Kimberley, where they occur in a train of parallel or bifurcating ridges with a mean wavelength of approximately 2.7–3 m and a mean height of 10–20 cm (Figures 6a–6e). The bedforms are relatively straight in planform with crests that trend ENE-WSW; the crests are sharp in cross-sectional profile. Not all crests are horizontal; some climb in elevation as much as 2 m from west to east (sol 0590 Mastcam image MR02483, not shown).

At least one bedform at Kimberley displays internal stratification that records reversing north-south displacements (Figure 6e). These north- and south-dipping beds intersect at the bedform crest in interleaved zigzags (Hunter & Rubin, 1983; Rubin & Carter, 2006a, Figures 18–20 and 64). All cross-strata within the bedform appear to have been deposited by that bedform, with no visible core of underlying south-dipping beds.

The 3-m bedforms at Kimberley occur at the top of the Square Top member of the Kimberley formation (Figure 2; and Rice et al., 2017, Figure 5). The overlying strata of the Dillinger member (Rice et al., 2017) contain a distinctive wavy bed (wavelength of 2.7 m) that draped the bedforms; subsequent erosion of the Dillinger beds exhumed the bedforms (Figure 6d).



Figure 8. Candidate wave ripples at Square Top, displayed in plan form, as is common on earth. Grain size is coarse sand (1–2 mm); wavelength is 3–4 cm. Sol 0584 MR02444. Image: NASA/Caltech-JPL/MSSS.

The rover did not take images with sufficient resolution to resolve or measure individual grains, but the bedforms are interbedded with sandstones, and the strata comprising the bedforms have the appearance of other sandstones observed by *Curiosity*. The surfaces of the bedforms appear spatially uniform (Figures 6 and 7b), with no visible patchiness or detectable concentration of coarser grains along the crests, suggesting that grain size is relatively uniform within these bedforms.

3.3.1.2. Interpreted Depositional Origin

Although some striations that are visible in satellite images are ridges of outcropping south-dipping beds, several characteristics indicate that many striations at Kimberley and Dingo Gap are preserved bedforms. First, internal stratification records reversing migration (Figure 6e) rather than a consistent southward dip. Second, some of the ridges bifurcate (e.g., the bedform labeled “4” in Figure 6b), as is typical of bedforms. Third, some striated regions (Figure 6b) are almost entirely covered with the layers of sediment, with little or no evidence that underlying strata crop out. Other areas of some striated outcrops are covered completely by thin lenses of cross-beds deposited by reversing bedforms that were not preserved completely (white ellipses in Figure 7d).

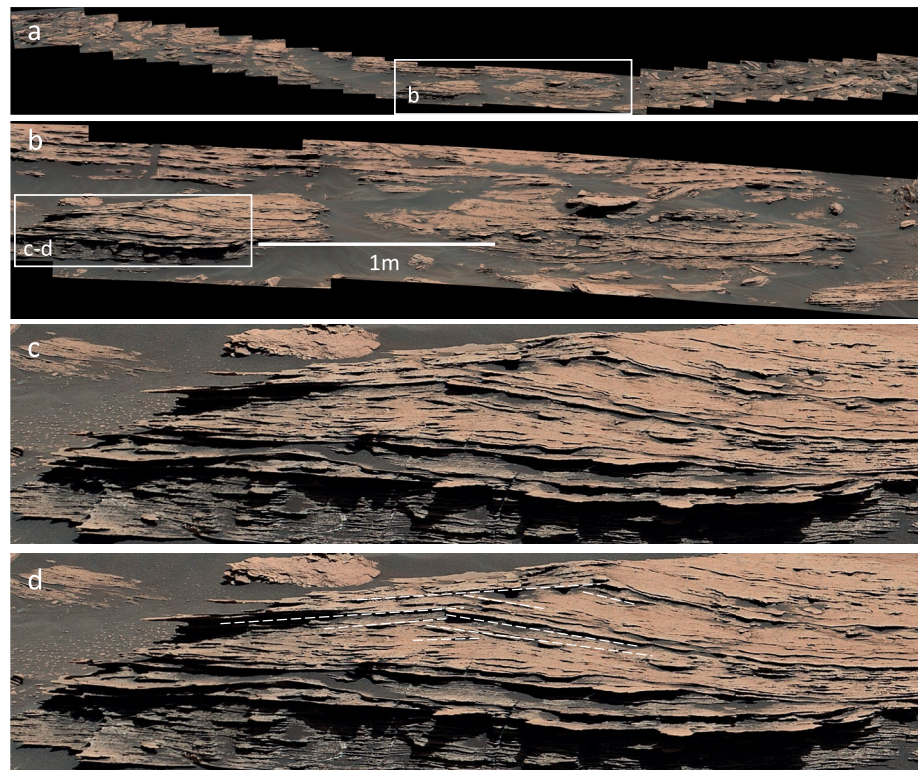


Figure 9. Candidate wave ripples at Hunda. Images: NASA/Caltech-JPL/MSSS. (a) Context image. The view is toward the south. The outcrop faces north at the right side of the image and toward the NW at the left side. The white rectangle shows the area enlarged in (b) Sol 2575 MR13526. (b) Possible wave ripple. To the right, the outcrop has several other beds with ripples or trough-shaped sets of cross-laminae. The area in the white rectangle is shown in (c) Sol 2575 MR13526. (c) Candidate wave ripple viewed approximately along the apparent bedform crests. The candidate ripple fills most of the image. The viewing angle is inclined downward at 10°. Crests shifted back and forth in the outcrop plane, with deposition on both flanks, and with an apparent net migration to the right. Morphology and wavelength are consistent with ripples in sand grain sizes ranging from 0.25 to 1 mm, and by waves generated by winds 2–4 times the threshold for aeolian sand transport. Sol 2572 MR13507. (d) Same area as (c) but dashed lines drawn to show reversals in bedform migration direction. Dashed lines show beds that were truncated when the bedform shifted to the left or right in the outcrop plane.

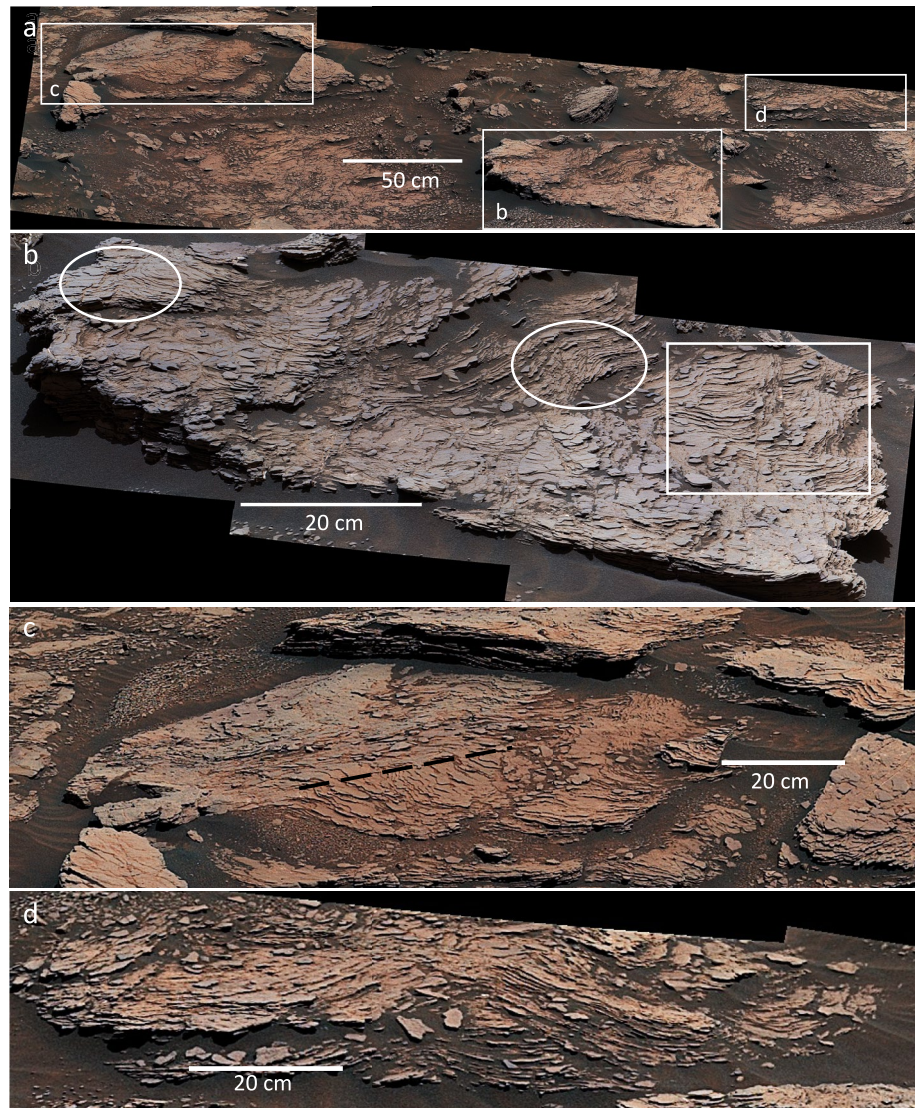


Figure 10. Candidate wave ripples at Voe and vicinity. Images: NASA/Caltech-JPL/MSSS. (a) Context image. The viewing direction is centered around southeast. White boxes show locations of b, c, and (d) Sol 2935 ML15306. (b) Voe viewed toward the southeast. The rock contains bedform crests and troughs. The crest of the symmetrical ripple at the upper left is oriented northwest-southeast. Climbing-ripple structures occur at the lower right. The ripple migration direction was away from the viewer, perhaps with a component of migration toward the right, although precise determination depends on post-depositional tilt. Sol 2936 ML15316. (c) Oblique section through relatively symmetrical ripples. The dashed line traces a ripple crest. This ripple is almost completely preserved, showing the planform geometry. The viewing direction is 112° , and the ripple crest appears to be rotated clockwise of this direction by a few tens of degrees, which indicates that the crest orientation is approximately northwest-southeast. The upper right of the image contains a ripple cross-section that shows relatively symmetrical deposition. Sol 2935 ML15306. (d) Cross-section through bedform, showing internal stratification that dips away from the ripple crest on partially preserved flanks. The ripple crest is nearly parallel to the viewing direction (152°). Sol 2935 ML15306.

We prefer an aeolian interpretation for these reversing bedforms at Kimberley for several reasons. First, modeled waves capable of generating 3-m-wavelength wave ripples require excessively high wind speeds (perhaps an order of magnitude greater than the threshold for aeolian transport, based on extrapolation of results in Figure 5). If the bedforms were anorbital wave ripples, which would be suggested by low bedform steepness (Wiberg & Harris, 1994), the necessary wind speeds would be even larger. In contrast, modern winds on Mars routinely form wind ripples with a modal wavelength of 1–3 m (Lapôtre et al., 2016). Second, the crests of some individual bedforms are inclined, with no systematic change in orientation, size, or morphology over an elevation range as

much as 2 m. This consistency in morphology would not be expected if the bedforms had been deposited in a subaqueous flow; winds are less likely to be affected by topography than subaqueous flow directions.

Aeolian ripples of this size and morphology can be caused by two factors: (1) coarse grain size (Sharp, 1963), or (2) low-density atmosphere (Lapôtre et al., 2016, 2018, 2021; Sullivan et al., 2020). Sand in coarse-grained ripples typically is segregated into patches of differing grain size, with coarser grains armoring the ripple crests; however, the surfaces of the Kimberley bedforms are exposed locally from trough to crest with no detectable difference in surface texture or differential erosion. Moreover, in an atmosphere with a pressure approaching that on Earth, these coarser grains need to be ~gravel-sized, which is clearly not the case at Kimberley. We therefore prefer the interpretation that the large ripple size was caused by low-atmospheric density. If we failed to recognize changes in texture caused by patches of coarse grains, however, then the ripples need not have formed in an atmosphere as thin as present day.

Lorenz et al. (2014) and Lapôtre et al. (2016) found that the wavelength of large martian aeolian ripples varies systematically with atmospheric density; the empirical relationship between ripple size and atmospheric density matches a scaling relationship that predicts the wavelength of subaqueous current ripples (Lapôtre et al., 2017), further suggesting an important role of Mars' low-density and high kinematic-viscosity atmosphere in setting the ripples' equilibrium size (Lapôtre et al., 2016). Two mechanisms have been proposed to explain the large size of aeolian ripples in a thin atmosphere. Durán Vinent et al. (2019) proposed that both the initiation and equilibrium size of large aeolian ripples arise from aerodynamic instabilities affected by atmospheric density. Sullivan et al. (2020) also argued that the large size on Mars arises from the thin atmosphere, but from a different mechanism: low wind dynamic pressures at ripple crests, allowing them to grow larger in thin atmospheres. Under both mechanisms, the formation of large ripples in well sorted sand thus requires a thin atmosphere (Lapôtre et al., 2021). Using the scaling relationship of Lapôtre et al. (2021), we find that the 2.7–3-m-wavelength ripples at Kimberley would have required an atmospheric density of $\sim 0.017 \text{ kg/m}^3$ (95% confidence interval: $0.01\text{--}0.03 \text{ kg/m}^3$), or close to modern-like ($\sim 0.02 \text{ kg/m}^3$).

The 3-m-wavelength bedforms at Kimberley have relatively straight crests, as has been reported for some large aeolian ripples on Mars (figure 4c of Lapôtre et al., 2018). Flows that produce straight-crested reversing bedforms in non-cohesive sand generally require at least two directional modes separated by an obtuse angle (Courrech du Pont et al., 2014; Reffet et al., 2010; Rubin, 2012; Rubin & Hunter, 1987; Rubin & Ikeda, 1990). Such winds are consistent with the reversing stratification in Figure 6e. Orientation of the large ripples at Kimberley requires that one of the directional modes of the winds that produced the large ripples must have had a substantial downslope component (south to north), and one component must have had a substantial upslope component (north to south). In this regard, the inferred winds are broadly consistent with both the present-day winds and those that formed dunes in the Stimson formation (Banham et al., 2018).

Heydari et al. (2020) interpreted the 3-m-wavelength bedforms at Kimberley as subaqueous dunes superimposed on antidunes in a northward megaflood flowing down Mt. Sharp. This interpretation of the 3-m-wavelength bedforms is unlikely for two reasons. First, the reversing bedforms are unlikely to be fluvial dunes because they reverse migration. (Subaqueous antidunes can reverse migration direction, but they have rounded crests; sharp crests induce flow separation, which is incompatible with flow over antidunes, and consequently the Kimberley bedforms are unlikely to be fluvial antidunes.) Second, it seems unlikely that a single short-duration (several days) flow proposed by Heydari et al. could have deposited the south-dipping beds, truncated them, and deposited the overlying bedforms, because at least one of the truncated beds has an eroded upper surface with a nearly vertical slope, suggesting that the bed was at least weakly cemented or consolidated before it was eroded (Figure 6f). It is unlikely that such cementation or consolidation could happen within a few days.

One of the puzzles arising from Grotzinger et al.'s (2015) (Figure 3b), mapping of OSOs is why their orientation is so consistent; orientation of striations would be expected to vary if the south-dipping beds were deposited on non-planar topography (as is common on deltas). In addition, even if the south-dipping beds were perfectly parallel, the trend of the traces of outcropping beds observed in satellite images should rotate where the outcrops have a slope perpendicular to the strike of the beds (i.e., a slope to the east or west). Our results suggest a different explanation for why the OSOs have a consistent orientation across individual outcrops and from one to another. If the striations were enhanced by aeolian processes—deposition of bedforms or preferential erosion of outcropping

beds with flow-parallel alignment—then orientation of striations would be more consistent than surface traces of outcropping beds.

In summary, the reversing 3-m-wavelength bedforms are interpreted to have formed by winds that reversed upslope-downslope in an atmosphere with a density approximately as low as that of present-day Mars.

3.3.1.3. *Interpreted Age*

The age of the lithified bedforms within the Bradbury group is important because it identifies the time when the atmosphere was thin. If the depositional model of Grotzinger et al. (2015) is correct, then deposition of the thin-atmosphere ripples at Kimberley was followed by deposition of more than 300 m of stratigraphically younger lake deposits of the Murray and Carolyn Shoemaker formations. On the other hand, if Heydari et al. (2020) are correct that the Murray formation is older than the ripples, or if Liu et al. (2021) are correct that the Murray formation is aeolian, then substantial lacustrine deposition cannot be demonstrated to post-date the thin atmosphere. Nevertheless, the thin atmosphere occurred prior to deposition of the ~1-m-thick Dillinger member, which has also been interpreted as a subaqueous or mixed subaqueous/aeolian deposit (Heydari et al., 2020; Le Deit et al., 2016; Rice et al., 2017). Thus, regardless of the age of the 3-m-wavelength ripples relative to the Murray formation, the atmosphere was thin—at least temporarily—prior to deposition of the subaqueous strata of the Dillinger member.

Grotzinger et al. (2015) based their argument that the Murray formation did not pre-date the Bradbury group in part on their interpretation that small deltas—visible as OSOs—were not deflected by pre-existing topography of the Murray formation. Our finding that orientation of striations can reflect aeolian processes on an ancient outcrop allows the possibility that orientation of deltas may have been more variable than the orientation of striations.

The conclusion that Mars' atmosphere was at least temporarily thin is consistent with previous work by Lapôtre et al. (2016) who suggested that low-atmospheric-density aeolian ripples in the Burns formation might have pre-dated lakes in Gale crater. They noted that their conclusion was uncertain because of possible errors in correlating ages between the two locations. The results presented here, however, do not require correlation between different locations; the thin atmosphere occurred prior to subaqueous deposition within the stratigraphic sequence at a single location (Kimberley).

3.4. Square Top

Square Top is a rock slab in the Square Top member of the Kimberley formation at Kimberley (Figure 8); Le Deit et al. (2016), (Figure 4c); Rice et al. (2017), (Figure 4a, right of center of their image). The slab is located at or near the top of the exposed Square Top member and—as precisely as can be determined—is stratigraphically in the same position or directly underlies the 3-m-wavelength ripples described above (Figure 2).

The upper bedding plane of the slab contains linear structures that resemble ripples. The relatively straight, continuous, planform geometry is consistent with wave ripples, with some “crests” extending almost across the entire slab; smaller-scale irregularities are consistent with an interference pattern formed by waves from multiple directions or by a unidirectional current combined with waves. Grotzinger et al. (2015) reported grains as coarse as 3.1 mm within the Square Top slab, and Le Deit et al. (2016) reported grain size of the Square Top member as very coarse sand (1–2 mm). The observed wavelength (3–4 cm) is at the lower size limit of modeled wave ripples in 1- and 2-mm sand (Figure 5).

This structure also resembles wind ripples, which become straight-crested because of along-crest ballistic grain splash (Rubin, 1992, 2012; Yizhaq et al., 2004). In this case, the smaller-scale irregularities would suggest a changing wind direction. Because the structures occur at or near the top of the Square Top member—the same stratigraphic horizon as the 3-m-wavelength aeolian ripples—the context is also suitable for aeolian ripples. Nevertheless, these structures remain viable candidates for wave ripples.

3.5. Hunda

3.5.1. Description

The Hunda outcrop (Bryk et al., 2020) occurs in the Knockfarril Hill member of the Carolyn Shoemaker formation at an elevation of $-4,120$ m; this is approximately 360 m higher in elevation than the thin-atmosphere ripples and Square Top in the Kimberley formation. Previous studies report that the Knockfarril Hill member contains widespread cross-bedding (Bryk et al., 2020; Caravaca et al., 2021; Fedo et al., 2020), representing a change from the underlying lacustrine depositional environment, with some publications suggesting that the Knockfarril Hill member is dominantly fluvial rather than lacustrine (Caravaca et al., 2021).

The Hunda outcrop contains two beds approximately 70 cm apart in elevation deposited by bedforms that are relatively symmetrical in cross-section and that have internal stratification that preserves deposition on both flanks (Figure 9). Mean wavelength of the bedforms measured in the outcrop plane is 79 cm, and height ranges up to 6 cm. The crests (viewed in 3-D software) are not orthogonal to the outcrop but are oriented at 60° – 70° to it. Correcting for this obliquity reduces the true wavelength to 68–75 cm. Viewing in three dimensions also shows that the bedforms are relatively symmetrical and not merely a coincidence of outcrop orientation causing asymmetrical bedforms to appear symmetrical. Laminae at the crest of one of these bedforms shows interleaving zigzags that record the left-right reversals of migration direction in the outcrop plane (Figure 9d).

The larger-scale depositional surface on which the Hunda bedforms formed was relatively flat in the plane of the outcrop (east-west), but beds dip into and out of the outcrop, indicating that the topography was not entirely planar. Cross-strata—including trough-shaped sets noted by Bryk et al. (2020)—indicate parts of the outcrop were deposited on larger-scale topography than the symmetrical bedforms. Hunda was viewed toward the south in a curving outcrop that faces toward the north (right side of Figure 9a) and northeast (left side of Figure 9a). The bedform in Figure 9c is viewed along a line of sight that plunges toward the south at an inclination of 10° . The southward dip is most obvious in another image from this location (Sol 2575 MR013527, not shown), although it is not known if some of the generally southward dip has been caused by post-depositional tilting.

3.5.2. Interpretation

A variety of lacustrine and fluvial processes might produce symmetrical reversing bedforms with some similarity to those in Hunda: reversing flows produced by waves in a lake; reversing flows caused by other processes such as seiches in a lake or pulsating eddies in a river; deposition on bedforms oriented parallel to flow in river or parallel to density currents in a lake; and deposition by antidunes. Although Hunda occurs in the dominantly fluvial Knockfarril Hill member, deposits at the mouth of a river can be subject to reworking by waves or wind, and changes in lake level or changes in location of rivers can cause fluvial, lacustrine, and aeolian beds to interfinger. Consequently, context is of little help in distinguishing between a wave-ripple origin and other possibilities.

The grain size of the bedforms at Hunda is unknown, but the ripple wavelength is consistent with orbital ripples formed in sand grain sizes ranging from 0.25 to 1 mm and by waves produced by winds twice or more the threshold for aeolian sand transport (Figure 5). In atmospheres of 6, 60, and 600 mbar, this corresponds to wind speeds (at 10 m above the bed) of 60, 30, and 9 m/s, respectively. The required speeds at 60 and 600 mbar are only slightly faster than *Curiosity*'s measurements reported by Newman et al. (2017), which as noted above excluded wind speeds greater than 20 m/s, were made closer to the bed where winds are weaker, and were collected only during the weak-wind season. The required wind speed at 6 mbar is 60 m/s, but despite being more than twice the speeds reported by Newman et al. (2017), such winds may have occurred occasionally, particularly during the windy season.

Waves are not the only kind of reversing flows that produce reversing bedforms. Reversing bedforms also arise in pulsating eddies in rivers (Rubin et al., 1990; Rubin & MacDonald, 1995; Rubin & Carter, 2006a, Figures 20, 28, 63, 64), and reversing bedforms might also be expected in reversing flows of impact- or landslide-generated tsunamis or seiches (Lacy et al., 2012; Moore et al., 2014; Shanmugam, 2012). In oceans on Earth, sediment transport can also be driven by internal waves impacting the continental margin (Cacchione & Southard, 1974), but we don't know that such a process in a small lake can cause symmetrical reversing flows capable of producing bedforms as large as those at Hunda.

Symmetrical bedforms with opposing cross-laminae arranged in zigzags at the crest can also originate on flow-parallel spurs on the lee sides of larger bedforms (defined loosely to include any kind of migrating sediment

ridge in air or water) even in relatively unidirectional flows (Rubin & Carter, 2006a, Figures 48–49, 59, 60). The southward plunge of Hunda's crest may reflect such geometry, but the structure of the outcrop and adjacent beds makes it difficult to demonstrate that these dips are original depositional dips rather than subsequent tilting. The presence of cross-bedding within individual blocks on the outcrop, however, indicates that original dips were not all horizontal and that other bedforms were present.

Symmetrical ripples with deposition on both flanks also form in density currents in glacial lakes (Jopling & Walker, 1968). The reversing bedforms at Hunda have sharp crests and are therefore unlikely to have formed as antidunes (as discussed for the 3-m-wavelength bedforms at Kimberley).

A classic outcrop for identifying wave ripples would be a bedding plane exposing many parallel ripples (as in Square Top, Figure 8) combined with a vertical cross-section to display internal stratification (lacking at Square Top). Not only can an extensive bedding-plane show the ripple planform shape, but if the bedding plane lacks larger-scale relief, many of the fluvial alternatives to waves can be excluded. For example, eddy-pulsation ripples require larger-scale channel topography. Some sets of cross-beds at Hunda, however, dip into and out of the outcrop making it difficult to exclude larger-scale topography in a north-south direction. In particular, we can't definitively exclude the possibility that the symmetrical bedforms were deposited on flow-parallel features of small bedforms migrating toward the south.

Even if the Hunda beds are dominantly subaqueous, an episode of subaerial exposure may have subjected sediment on the bed to aeolian reworking. This happens routinely in modern settings and can be difficult to identify even in high-quality outcrops in modern sands that can be excavated by hand in three dimensions (Rubin et al., 1990). The wavelength and height of the Hunda bedforms are within the range of modern aeolian ripples on Mars.

In summary, the symmetrical bedforms at Hunda remain viable candidates for wave ripples formed at a river mouth or formed on the lake floor in a lacustrine interbed in the dominantly fluvial Knockfarril Hill member, but we cannot reject the hypotheses that the symmetrical bedforms were deposited by flow-parallel topographic features on other bedforms or formed by non-wave reversing flows.

3.6. Voe

3.6.1. Description

The Voe outcrop (Figure 10) is located 700 m east of Hunda and 8 m higher in elevation. The bedforms in Voe are similar in some regards to those in Hunda. Like those at Hunda, they occur in the Knockfarril Hill member, they are several decimeters in wavelength, and—with one exception—the bedforms are not preserved in planform but rather are defined by cross-laminae that converge at the crests (Figures 10b–10d). The exception is a single bedform that is exposed in a low-angle oblique section that is nearly conformable with the bedform morphology (Figure 10c).

The ripple crests in Voe are not all parallel. The ripples in Figures 10c and 10d, and the upper left corner of 8b are oriented approximately in the viewing direction (toward the southeast), whereas the ripple near the center of Figure 10b is rotated counterclockwise from that direction. The crest-to-trough distance of the ripple at the upper left in Figure 10b is approximately 20 cm, and the symmetrical morphology suggests that a full wavelength would span approximately 40 cm.

The symmetrical bedforms in Voe overlie four sets of climbing-ripple cross-laminae (white rectangle in Figure 10b). Unlike the relatively symmetrical candidate wave ripples that aggraded with little or no net migration (white ellipses in Figure 10b), the underlying climbing ripples were deposited by a train of four ripples that consistently migrated approximately in the viewing direction (southeast), and therefore had crests oriented north-east-southwest. Voe thus preserves migrating ripples with one orientation overlain by reversing ripples with an approximately orthogonal orientation.

The symmetrical bedforms occur on a bed with larger-scale topography. Those at the upper left in Figure 10b and the upper right in Figure 10c appear to have formed on a plane that was nearly parallel to the line of sight, whereas the beds near the center of the figure dip more steeply toward the left (confirmed viewing stereo images).

3.6.2. Interpretation

Winds that only slightly exceeded the threshold of aeolian transport would have been capable of generating suitable waves to make 40-cm-wavelength orbital wave ripples (Figure 5). In atmospheres of 6, 60, and 600 mbar, this corresponds to wind speeds of 30, 15, and 4 m/s, respectively. Winds of these speeds are within the realm of what might be expected.

Voe is underlain by deposits of subaqueous ripples that migrated in a consistent direction (i.e., they were formed by currents or combined waves and currents rather than by symmetrical waves without currents). The nearly orthogonal orientation of the possible wave ripples and the underlying migrating ripples makes it unlikely that both sets were formed by waves from the same direction, even if combined currents were involved (Lacy et al., 2007).

On a spatial scale of a meter or two, the topography on which the symmetrical bedforms originated was not planar. If the bedforms are wave ripples, then their differing orientations may have arisen from the non-planar topography. The exposure at Voe is restricted in all three dimensions, making it impossible to determine whether or not the observed non-planar topography was part of a larger subaqueous channel.

As is the case for Square Top and Hunda, the bedforms at Voe remain viable candidates for wave ripples, but we cannot exclude a variety of alternatives. Even if waves are perhaps our preferred interpretation for one or more of these examples, we do not have a sufficiently high confidence that they are wave ripples to use them to constrain Mars' climate history.

4. Discussion

4.1. Atmosphere

Mars has a dry low-density atmosphere, but the planet has abundant geomorphic, sedimentologic, and geochemical evidence of an ancient wet climate that presumably required a denser atmosphere (Carr & Head, 2010; Catling, 2009; Grotzinger et al., 2015; Malin & Edgett, 2000). Climate models (Forget et al., 2013) and lack of widespread fluvial activity in the last 3 billion years (Carr & Head, 2010) suggest that Mars' atmosphere had thinned by then. The precise nature of the transition, however, remains uncertain. Some studies suggest that the transition from an early, warm, dense, wet atmosphere occurred with episodic fluctuations rather than monotonic change (Wordsworth, 2016). Palucis et al. (2016) suggested that “regional climatic events switched on and off suddenly”, with lakes in Gale crater persisting for perhaps 10^5 years, and Rapin et al. (2021) argued that rather than a monotonic drying, the climate fluctuated multiple times between wet and dry.

The 3-m-wavelength aeolian ripples at Kimberley identify a time when atmospheric density was approximately as thin as at the present day. The low atmospheric pressure applies to all atmospheric constituents—not just to a low partial pressure of individual components (Bristow et al., 2017). The thin-atmosphere ripples predate the subaqueous beds of the Dillinger member (Rice et al., 2017) and therefore predate cessation of subaqueous deposition in Gale crater, as suggested by Lapôtre et al. (2016).

One unresolved question regarding the OSOs is what proportion of them underwent aeolian erosion and deposition prior to burial by subaqueous strata, as at Kimberley. The OSOs at Dingo Gap, Emu Point, Kylie, and Kimberley all have preserved bedforms or lenses of cross-beds with reversing dips of a scale appropriate for deposition by large aeolian ripples, but Kimberley is the only location where we can demonstrate that the deposits of the large aeolian ripples are older than adjacent topographically higher subaqueous beds (because the overlying subaqueous beds drape the rippleform topography as shown in Figure 6d). Other outcrops of ancient large aeolian ripples or their remnants (Dingo Gap and Kylie) also have adjacent topographically higher subaqueous beds, but without visible draping of bedforms, we cannot exclude the possibility that the large aeolian ripples at those locations were deposited more recently in depressions that had been eroded into the outcrops. If the OSOs visited by *Curiosity* are representative of the more than 700 OSOs that the rover did not visit—and if the OSOs decrease in age southward and upward as proposed by Grotzinger et al.—more than 100 fluctuations in lake level are required to account for the repeated sequences of deposition of deltas fed from the north followed by deposition of aeolian bedforms that together define OSOs. Alternatively, if Kimberley is an aberration and other OSOs do not contain aeolian large ripples buried by subaqueous beds, then repeated subaerial and subaqueous deposition

are not required. Similarly, if the OSOs were deposited on a single erosional surface that dipped northward as proposed by Heydari et al. (2020), then only one thin-atmosphere event is required.

4.2. Wave Ripples

Aeolian action in Gale crater is demonstrated by active aeolian ripples and dunes (Bridges et al., 2017; Lapôtre & Rampe, 2018; Silvestro et al., 2013), widespread ancient aeolian deposits (Banham et al., 2018; Rapin et al., 2021), and sand-blasted rocks and landscapes (Day & Kocurek, 2016). Wave modeling for the inferred lake conditions (ice-free; fetch 20 km; depth 10 m) suggests that regardless of atmospheric density, winds capable of causing aeolian sand transport would have been sufficient to generate waves that transported sand near the shore. For winds ranging from $\frac{1}{4}$ of the threshold of aeolian sand transport to 4 times the threshold, the predicted ripple wavelengths range from a few cm to approximately 1 m, increasing with wind stress and grain size.

The sedimentary structures described above are the best candidates for wave ripples that we have identified during *Curiosity's* traverse across more than 10 km of inferred lacustrine deposits. Although some beds contain ripples formed by currents (Stack et al., 2019) or contain ripples of unknown origin, thick sections of the Murray formation are dominated by finely laminated beds devoid of any ripples. These beds are interpreted as lacustrine sediment that accumulated by fallout from suspension (Edgar et al., 2020; Fedo et al., 2018). Many hypotheses might explain why wave ripples are absent in these flat-laminated beds: (a) the lake was too deep for waves to rework the bed, (b) sediment was too fine to form ripples large enough to be detected, (c) the lake surface was covered with ice, (d) the Murray formation is aeolian rather than lacustrine (Liu et al., 2021), or (5) winds were weaker when a lake was present. These hypotheses are considered in the following paragraphs.

It is entirely plausible that some lacustrine settings in Gale crater were too deep for waves to rework the bed or that the bed was locally too fine to form wave ripples large enough to be observed; both conditions are most likely to have been met in deeper more distal locations in a lake. On the other hand, the presence of lowstand deposits with desiccation cracks in the Murray formation led Stein et al. (2018) to suggest that the lake underwent widespread fluctuations in lake level—not just at margins of the lake. Such widespread fluctuations would necessarily make the lake shallow at times, although associated wave ripples have not been identified.

Grotzinger et al. (2015) argued that a lack of recognized glacial and periglacial features (frost wedges, dropstones, glacial tills) suggests a lack of ice on the lake. Using a climate model that balanced water input to the lake, freezing on the bottom of an ice cover, and sublimation of the upper ice surface, Kling et al. (2020) calculated that an ice cover of a few meters or tens of meters would have been sufficient to maintain a lake in Gale crater under conditions of an annual mean temperature of 235–270 K and an atmosphere of 0.5 bar. An ice thickness of 30 m would provide enough hydrostatic pressure to prevent underlying water from boiling under frigid temperatures even in an atmosphere thinner than present. Such thin ice would be insufficient to produce flowing glaciers (or glacial deposits such as tills). Kling et al. also noted that freeze-thaw weathering might be reduced where melting occurred infrequently. It is further plausible that at very low atmospheric pressures and low temperatures frost wedging would be eliminated because the sediment would be vacuum freeze-dried before ice could melt and refreeze; such vacuum freeze-drying has been proposed as a technique to preserve sediment cores and prevent them from cracking (Enevold et al., 2019).

Kling et al. (2020) noted that their model of an ice-covered lake does not account for the observed fluvial sedimentary structures. They cite Kite, Halevy et al. (2013) who proposed that fluvial activity might be episodic, but we do not know if it is possible to develop a model that balances these opposing constraints (cold and dry to prevent frost-wedging and wet to provide fluvial inputs of sediment).

Liu et al. (2021) argued that the Murray formation is dominantly aeolian rather than lacustrine. This would explain why parts of the section are devoid of wave ripples, but their argument for aeolian deposition is based in part on the presence of cross-lamination and cross-bedding. Such stratification, however, is not atypical of lakes, where it forms not only as a result of waves as discussed here, but also by currents caused by inflowing rivers (Edgar et al., 2020; Stack et al., 2019), wind, density (Normandeau et al., 2016), and tsunamis (Lawton et al., 2005; Moore et al., 2014; Shanmugam, 2012). We are, therefore, skeptical that the presence of cross-bedding is inconsistent with lacustrine deposits. Moreover, aeolian interbeds within a dominantly lacustrine deposit would not be surprising, given that desiccation cracks are present (Stein et al., 2018).

A lack of sand-transporting winds when the lake was present cannot be ruled out from geologic observations, but there is no reason to suspect that winds were weaker when a lake was present.

As noted by Fedo et al. (2020), the cross-stratification in the Knockfarril Hill unit represents a distinct change from the underlying 200 m of strata lacustrine beds, suggesting a change in depositional environment. A shallowing of the lake or reduction of ice cover would be consistent with enabling formation of wave ripples at Hunda and Voe.

If the ripples at either of the Knockfarril Hill outcrops are, in fact, wave ripples, their presence would demonstrate that the lake was ice-free at that time. One possibility is that the atmospheric density was at times great enough for water in an ice-free lake to exist as a non-boiling liquid (lake surface temperature above 273 K and atmospheric pressure that need not have exceeded a few tens of mbar) as shown by Kling et al. (2020) and Nair and Unnikrishnan (2020). Alternatively, the lake may usually have been covered with ice, with wave ripples forming only when the ice was absent (Knockfarril Hill member). Models suggest that in a cold low-density atmosphere a 100-m-deep lake would evaporate within tens to thousands of years (Kling et al., 2020). Although this is short on a geological time scale, the time required to form wave ripples is only minutes or hours.

Evaporation of lake water would likely have increased the concentrations of salts, which allows water to remain liquid over a wider range of temperatures, both by decreasing the freezing point and raising the boiling point (Nair & Unnikrishnan, 2020). Evidence of high salinity in the lake has been demonstrated for some beds in the Murray formation (Rapin et al., 2021), but not for the beds with candidate ripples. Brine concentrations even at unsaturated levels, however, would increase the stability of range of liquid water without necessarily depositing evaporites.

In summary, wave ripples may have been present during different episodes of lake formation and deposition in Gale crater; if so, that lake must then have been free of ice. To be ice-free, the temperature must have been warm enough for water to be liquid, and atmospheric pressure must have been high enough to prevent boiling at a rate that could prevent formation of waves. In a low-salinity lake, those conditions would be met where atmospheric pressures exceed 7 mbar at 273 K or exceed a few tens of mbar at temperatures of 290 K. Higher salinity would expand the range of conditions at water would remain liquid and waves might form.

5. Conclusions

1. Regardless of atmospheric density, winds that were sufficient to initiate aeolian transport of sand would have generated waves on an ice-free lake with the modeled dimensions (fetch of 20 km and depth of 10 m). Those waves would have been capable of transporting all grain sizes of sand near the shoreline and would have been sufficient to produce wave ripples.
2. The rover observed a handful of sedimentary structures that exhibit some characteristics of wave ripples and that are a size consistent with formation by modeled waves. Those at Square Top, Hunda, or Voe remain viable candidates for wave ripples.
3. Of the lacustrine beds with visible stratification, non-rippled beds are more common than beds with any kind of ripples. The most likely possibilities for inhibiting formation of wave ripples are that the lake was too deep, too small, covered with ice, or that *Curiosity's* preferentially sampled distal fine-grained lacustrine deposits and largely avoided the nearshore regions, where wave action is enhanced.
4. The 3-m-wavelength ripples at Kimberley—if they consist of well sorted sand as appears to be the case—are best interpreted as large aeolian ripples that formed in an atmosphere as thin as at present. They formed in winds that reversed with upslope-downslope (north-south) components, as they do today.
5. At Kimberley these thin-atmosphere ripples are overlain by subaqueous beds. This sequence demonstrates that the atmosphere was thin at least temporarily before subaqueous deposition ceased in Gale crater.
6. At Kimberley and Dingo Gap, many orbital striations are preserved bedforms rather than outcropping south-dipping strata. Grotzinger et al. (2015) identified 741 outcrops with orbital striations. It remains unknown how many of these outcrops include thin-atmosphere aeolian ripples or were enhanced by aeolian erosion. It is also unknown how many of the OSOs are overlain by younger subaqueous deposits.

Data Availability Statement

All Mastcam images taken by the rover are archived at the NASA Planetary Data Systems and are available at <https://pds-geosciences.wustl.edu/missions/msl/> (Malin, 2013). The MSL Analyst's Notebook (Stein et al., 2016) is available at <https://an.rsl.wustl.edu/msl/mslbrowser/an3.aspx>. Mastcam mosaics were processed by the Mastcam team at Malin Space Science Systems. HiRISE satellite images (McEwen, 2007) are available at doi.org/10.17189/1520303, and an image of Kimberley is available at <https://www.uahirise.org/releases/msl-kimberley.php>.

Acknowledgments

The SWAN model computational grid, bathymetry, boundary conditions, and numerical and physical parameters are provided in Stevens and Rubin (2022). Part of this research was carried out at the Jet Propulsion Laboratory, California Institute of Technology, under a contract with the National Aeronautics and Space Administration (80NM0018D0004), French Agence Nationale de la Recherche (ANR) under the contract ANR-16-CE31-0012 entitled Mars-Prime, and by the French space agency CNES under convention CNES 180027. Any use of trade, firm, or product names is for descriptive purposes only and does not imply endorsement by the U.S. Government.

References

- Andreotti, B., Claudin, P., Iversen, J. J., Merrison, J. P., & Rasmussen, K. R. (2021). A lower-than-expected saltation threshold at Martian pressure and below. *Proceedings of the National Academy of Sciences*, 118, 5. <https://doi.org/10.1073/pnas.2012386118>
- Baker, M. M., Lapôtre, M. G. A., Minitti, M. E., Newman, C. E., Sullivan, R., Weitz, C. M., et al. (2018). The Bagnold dunes in southern summer: Active sediment transport on Mars observed by the Curiosity rover. *Geophysical Research Letters*, 45(17), 8853–8863. <https://doi.org/10.1029/2018gl079040>
- Banfield, D., Donelan, M., & Cavaleri, L. (2015). Winds, waves and shorelines from ancient martian seas. *Icarus*, 250, 368–383. <https://doi.org/10.1016/j.icarus.2014.12.001>
- Banham, S. G., Gupta, S., Bryk, A. B., Rubin, D. M., Bryk, A. B., Edgett, K. S., et al. (2021). *Winds of change: A hesperian record of seasonal to millennial-scale wind fluctuations, recorded in the aeolian Stimson formation sandstones in Gale Crater, Mars*. National Astronomical Meeting 2021. Retrieved from <https://nam2021.org/friday/details/26/31>
- Banham, S. G., Gupta, S., Rubin, D. M., Watkins, J. A., Sumner, D. Y., Edgett, K. S., et al. (2018). Ancient Martian aeolian processes and palaeomorphology reconstructed from the Stimson formation on the lower slope of Aeolis Mons, Gale crater, Mars. *Sedimentology*, 65(4), 993–1042. <https://doi.org/10.1111/sed.12469>
- Booij, N., Ris, R. C., & Holthuijsen, L. H. (1999). A third-generation wave model for coastal regions, Part I—Model description and validation. *Journal of Geophysical Research*, 104(C4), 7649–7666. <https://doi.org/10.1029/98jc02622>
- Bridges, N. T., Sullivan, R., Newman, C. E., Navarro, S., Van Beek, J., Ewing, R. C., et al. (2017). Martian aeolian activity at the Bagnold dunes, Gale crater: The view from the surface and orbit. *Journal of Geophysical Research: Planets*, 122(10), 2077–2110. <https://doi.org/10.1002/2017je005263>
- Bristow, T. F., Haberle, R. M., Blake, D. F., Des Marais, D. J., Eigenbrode, J. L., Fairén, A. G., et al. (2017). Low Hesperian PCO₂ constrained from in situ mineralogical analysis at Gale Crater, Mars. *Proceedings of the National Academy of Sciences*, 114(9), 2166–2170. <https://doi.org/10.1073/pnas.1616649114>
- Bryk, A. B., Dietrich, W. E., Fox, V. K., Bennett, K. A., Banham, S. G., Lamb, M. P., et al. (2020). The stratigraphy of Central and Western butte and the Greenheugh pediment contact. *51st lunar and planetary science conference*. (p. 2612).
- Cacchione, D. A., & Southard, J. B. (1974). Incipient sediment movement by shoaling internal gravity waves. *Journal of Geophysical Research*, 79(15), 2237–2242. <https://doi.org/10.1029/jc079i015p02237>
- Caravaca, G., Mangold, N., Dehouck, E., Schieber, J., Bryk, A., Fedo, C., et al. (2021). Evidence of depositional settings variation at the Jura/ Knockfarril Hill members transition in the Glen Torridon region (Gale crater, Mars). In *52nd lunar and planetary science conference*. LPI Contribution No. 1455.
- Carr, M. H., & Head, J. W. III. (2010). Geologic history of Mars. *Earth and Planetary Science Letters*, 294(3–4), 185–203. <https://doi.org/10.1016/j.epsl.2009.06.042>
- Catling, D. C. (2009). Atmospheric evolution of Mars. In V. Gornitz (Ed.), *Encyclopedia of paleoclimatology and ancient environments* (pp. 66–75). Springer.
- Courech du Pont, S., Narteau, C., & Gao, X. (2014). Two modes for dune orientation. *Geology*, 42(9), 743–746. <https://doi.org/10.1130/G35657.1>
- Cummings, D. I., Dumas, S., & Dalrymple, R. W. (2009). Fine-grained versus coarse-grained wave ripples generated experimentally under large-scale oscillatory flow. *Journal of Sedimentary Research*, 79(2), 83–93. <https://doi.org/10.2110/jsr.2009.012>
- Day, M., & Kocurek, G. (2016). Observations of an aeolian landscape: From surface to orbit in Gale Crater. *Icarus*, 280, 37–71. <https://doi.org/10.1016/j.icarus.2015.09.042>
- Deltares (2018). *Delft3D-Wave, Simulation of short-crested waves with SWAN* (p. 198). User Manual. Deltares.
- Dietrich, W. E. (1982). Settling velocity of natural particles. *Water Resources Research*, 18(6), 1615–1626. <https://doi.org/10.1029/WR018i006p01615>
- Dumas, S., Arnott, R. W. C., & Southard, J. B. (2005). Experiments on oscillatory-flow and combined-flow bed forms: Implications for interpreting parts of the shallow-marine sedimentary record. *Journal of Sedimentary Research*, 75(3), 501–513. <https://doi.org/10.2110/jsr.2005.039>
- Duran Vincent, O., Andreotti, B., Claudin, P., & Winter, C. (2019). A unified model of ripples and dunes in water and planetary environments. *Nature Geoscience*, 12(44), 345–350. <https://doi.org/10.1038/s41561-019-0336-4>
- Edgar, L. A., Fedo, C. M., Gupta, S., Banham, S. G., Fraeman, A. A., Grotzinger, J. P., et al. (2020). A lacustrine paleoenvironment recorded at Vera Rubin ridge, Gale crater: Overview of the sedimentology and stratigraphy observed by the Mars Science Laboratory Curiosity rover. *Journal of Geophysical Research: Planets*, 125(3), e2019JE006307. <https://doi.org/10.1029/2019JE006307>
- Edgar, L. A., Gupta, S., Rubin, D. M., Lewis, K. W., Kocurek, G. A., Anderson, R. B., et al. (2017). Shaler: In situ analysis of a fluvial sedimentary deposit on Mars. *Sedimentology*, 65(1), 96–122. <https://doi.org/10.1111/sed.12370>
- Enevold, R., Flintoft, P., Tjelliden, A. K. E., & Kristiansen, S. M. (2019). Vacuum freeze-drying of sediment cores: An optimized method for preserving archaeostratigraphic archives. *Antiquity*, 93, 1–4. <https://doi.org/10.15184/aqy.2019.98>
- Fedo, C. M., Grotzinger, J. P., Bryk, A., Bennett, K., Fox, V., Stein, N., et al. (2020). Ground-based stratigraphic correlation of the Jura and Knockfarril Hill members of the Murray formation, Gale Crater: Bridging the vera Rubin ridge — glen torridon divide. In *51st lunar and planetary science conference*. LPI Contribution No. 2345.
- Fedo, C. M., Grotzinger, J. P., Gupta, S., Fraeman, A., Edgar, L., Edgett, K., et al. (2018). Sedimentology and stratigraphy of the Murray formation, Gale crater, Mars. In *49th lunar and planetary science conference*. LPI Contribution No. 2078.
- Forget, F., Wordsworth, R., Millour, E., Madeleine, J.-B., Kerber, L., Leconte, J., et al. (2013). 3D modelling of the early martian climate under a denser CO₂ atmosphere: Temperatures and CO₂ ice clouds. *Icarus*, 222(1), 81–99. <https://doi.org/10.1016/j.icarus.2012.10.019>

- Grant, W. D., & Madsen, O. S. (1982). Movable bed roughness in unsteady oscillatory flow. *Journal of Geophysical Research*, 87(C1), 469–481. <https://doi.org/10.1029/JC087iC01p00469>
- Grotzinger, J. P., Gupta, S., Malin, M. C., Rubin, D. M., Schieber, J., Siebach, K., et al. (2015). Deposition, exhumation, and paleoclimatology of an ancient lake deposit, Gale Crater, Mars. *Science*, 350(6257). <https://doi.org/10.1126/science.aac7575>
- Heydari, E., Schroeder, J. F., Calef, F. J., Van Beek, J., Rowland, S. K., Parker, T. J., et al. (2020). Deposits from giant floods in Gale crater and their implications for the climate of Mars. *Scientific Reports*, 10(1), 19099. <https://doi.org/10.1038/s41598-020-75665-7>
- Hunter, R. E., & Rubin, D. M. (1983). Interpreting cyclic crossbedding, with an example from the Navajo Sandstone. In M. E. Brookfield, & T. S. Ahlbrandt (Eds.), *Eolian sediments and processes* (pp. 429–454). Elsevier.
- Jopling, A. V., & Walker, R. G. (1968). Morphology and origin of ripple-drift cross-lamination with examples from the Pleistocene of Massachusetts. *Journal of Sedimentary Research*, 38(4), 971–984. <https://doi.org/10.1306/74D71ADC-2B21-11D7-8648000102C1865D>
- Kite, E. S., Halevy, I., Kahre, M. A., Wolff, M. J., & Manga, M. (2013). Seasonal melting and the formation of sedimentary rocks on Mars, with predictions for the Gale Crater mound. *Icarus*, 223(1), 181–210. <https://doi.org/10.1016/j.icarus.2012.11.034>
- Kite, E. S., Lewis, K. W., Lamb, M. P., Newman, C. E., & Richardson, M. I. (2013). Growth and form of the mound in Gale Crater, Mars: Slope-wind enhanced erosion and transport. *Geology*, 41(5), 543–546. <https://doi.org/10.1130/G3309.1>
- Kling, A. M., Haberle, R. M., McKay, C. P., Bristow, T. F., & Rivera-Hernandez, F. (2020). Subsistence of ice-covered lakes during the Hesperian at Gale crater, Mars. *Icarus*, 338, 113495. <https://doi.org/10.1016/j.icarus.2019.113495>
- Kok, J. F. (2010). Difference in the wind speeds required for initiation versus continuation of sand transport on Mars: Implications for dunes and dust storms. *Physical Review Letters*, 104(7), 074502. <https://doi.org/10.1103/physrevlett.104.074502>
- Lacy, J. R., Rubin, D. M., & Buscombe, D. (2012). Currents, drag, and sediment transport induced by a tsunami. *Journal of Geophysical Research*, 117(C9), C09028. <https://doi.org/10.1029/2012JC007954>
- Lacy, J. R., Rubin, D. M., Ikeda, H., Mokudai, K., & Hanes, D. M. (2007). Bed forms created by simulated waves and currents in a large flume. *Journal of Geophysical Research*, 112(C10), C10018. <https://doi.org/10.1029/2006JC003942>
- Lamb, M. P., Fischer, W. W., Raub, T. D., Perron, J. T., & Myrow, P. M. (2012). Origin of giant wave ripples in snowball Earth cap carbonate. *Geology*, 40(9), 827–830. <https://doi.org/10.1130/g33093.1>
- Lapôtre, M. G. A., Ewing, R. C., & Lamb, M. P. (2021). An evolving understanding of enigmatic large ripples on Mars. *Journal of Geophysical Research: Planets*, 12(2), e2020JE006729. <https://doi.org/10.1029/2020je006729>
- Lapôtre, M. G. A., Ewing, R. C., Lamb, M. P., Fischer, W. W., Grotzinger, J. P., Rubin, D. M., et al. (2016). Large wind ripples on Mars: A record of atmospheric evolution. *Science*, 353(6294), 55–58. <https://doi.org/10.1126/science.aaf3206>
- Lapôtre, M. G. A., Ewing, R. C., Weitz, C. M., Lewis, K. W., Lamb, M. P., Ehlmann, B. L., & Rubin, D. M. (2018). Morphologic diversity of martian ripples: Implications for large-ripple formation. *Geophysical Research Letters*, 45(19), 10229–10239. <https://doi.org/10.1029/2018GL079029>
- Lapôtre, M. G. A., Lamb, M. P., & McElroy, B. (2017). What sets the size of current ripples? *Geology*, 45(3), 243–246. <https://doi.org/10.1130/G38598.1>
- Lapôtre, M. G. A., & Rampe, E. B. (2018). Curiosity's investigation of the Bagnold dunes, Gale crater: Overview of the two-phase scientific campaign and introduction to the special collection. *Geophysical Research Letters*, 45(19), 10200–10210. <https://doi.org/10.1029/2018GL079032>
- Lawton, T. F., Shipley, K. W., Aschoff, J. L., Giles, K. A., & Vega, F. J. (2005). Basinward transport of Chicxulub ejecta by tsunami-induced backflow, La Popa basin, northeastern Mexico, and its implications for distribution of impact-related deposits flanking the Gulf of Mexico. *Geology*, 33(2), 81–84. <https://doi.org/10.1130/G21057.1>
- Le Deit, L., Mangold, N., Forni, O., Cousin, A., Lasue, J., Schroder, S., et al. (2016). The potassic sedimentary rocks in Gale Crater, Mars, as seen by ChemCam on board Curiosity. *Journal of Geophysical Research: Planets*, 121(5), 784–804. <https://doi.org/10.1002/2015JE004987>
- Liu, J., Michalski, J. R., & Zhou, M.-F. (2021). Intense subaerial weathering of eolian sediments in Gale crater, Mars. *Science Advances*, 7(32), eabh2687. <https://doi.org/10.1126/sciadv.abh2687>
- Lorenz, R. D., Bridges, N. T., Rosenthal, A. A., & Donkor, E. (2014). Elevation dependence of bedform wavelength on Tharsis Montes, Mars: Atmospheric density as a controlling parameter. *Icarus*, 230, 77–80. <https://doi.org/10.1016/j.icarus.2013.10.026>
- Malin, M. C., & Edgett, K. S. (2000). Sedimentary rocks of early Mars. *Science*, 290(5498), 1927–1937. <https://doi.org/10.1126/science.290.5498.1927>
- Malin, M. C., Ravine, M., Caplinger, M., Ghaemi, T., Schaffner, J., Maki, J., et al. (2017). The Mars Science Laboratory (MSL) mast cameras and descent imager: Investigation and instrument descriptions. *Earth and Space Science*, 4, 506–539. <https://doi.org/10.1002/2016EA000252>
- Malin, M. V. (2013). MSL Mars mast camera decompressed, radiometrically calibrated, color corrected, and geometrically linearized validated image data [Data set]. NASA Planetary Data System. <https://doi.org/10.17189/1520328>
- McEwen, A. (2007). MRO Mars high resolution imaging science experiment Reduced Data Record v1.1. *NASA Planetary Data System*. <https://doi.org/10.17189/1520303>
- Moore, J. G., Schweickert, R. A., & Kitts, C. A. (2014). Tsunami-generated sediment wave channels at Lake Tahoe, California–Nevada, USA. *Geosphere*, 10(4), 757–768. <https://doi.org/10.1130/ges01025.1>
- Nair, C. P. R., & Unnikrishnan, V. (2020). Stability of the liquid water phase on Mars: A thermodynamic analysis considering martian atmospheric conditions and perchlorate brine solutions. *ACS Omega*, 5(16), 9391–9397. <https://doi.org/10.1021/acsomega.0c00444>
- Newman, C. E., Gómez-Elvira, J., Richardson, M. I., Marín, M., Navarro, S., Torres, J., et al. (2017). Winds measured by the Rover Environmental Monitoring System (REMS) during the Mars Science Laboratory (MSL) rover's Bagnold Dunes campaign and comparison with numerical modeling using MarsWRF. *Icarus*, 291, 203–231. <https://doi.org/10.1016/j.icarus.2016.12.016>
- Nikuradse, J. (1933). Laws of flow in rough pipes (1950 translation). *National Advisory Committee on Aeronautics*. Technical Memorandum No 1292.
- Normandeau, A., Lajeunesse, P., Poiré, A. G., & Francus, P. (2016). Morphological expression of bedforms formed by supercritical sediment density flows on four fjord-lake deltas of the south-eastern Canadian shield (Eastern Canada). *Sedimentology*, 63(7), 2106–2129. <https://doi.org/10.1111/sed.12298>
- Palucis, M. C., Dietrich, W. E., Williams, R. M. E., Hayes, A. G., Parker, T., Sumner, D. Y., et al. (2016). Sequence and relative timing of large lakes in Gale crater (Mars) after the formation of Mount Sharp. *Journal of Geophysical Research: Planets*, 121(3), 472–496. <https://doi.org/10.1002/2015JE004905>
- Pedocchi, F., & Garcia, M. H. (2009). Ripple morphology under oscillatory flow: 2. Experiments. *Journal of Geophysical Research*, 114(C12), C12015. <https://doi.org/10.1029/2009jc005356>
- Rapin, W., Dromart, G., Rubin, D., Le Deit, L., Mangold, N., Edgar, L. A., et al. (2021). Alternating wet and dry depositional environments recorded in the stratigraphy of Mount Sharp at Gale crater, Mars. *Geology*, 49, 842–846. <https://doi.org/10.1130/G48519.1>
- Reffet, E., Courrech du Pont, S., Hersen, P., & Douady, S. (2010). Formation and stability of transverse and longitudinal dunes. *Geology*, 38(6), 491–494. <https://doi.org/10.1130/g30894.1>

- Rice, M. S., Gupta, S., Treiman, A. H., Stack, K. M., Calef, F., Edgar, L. A., et al. (2017). Geologic overview of the Mars Science Laboratory rover mission at the Kimberley, Gale crater, Mars. *Journal of Geophysical Research: Planets*, 122(1), 2–20. <https://doi.org/10.1002/2016je005200>
- Rubin, D. M. (1992). Use of forecasting signatures to help distinguish periodicity, randomness, and chaos in ripples and other spatial patterns. *Chaos*, 2(4), 525–535. <https://doi.org/10.1063/1.165894>
- Rubin, D. M. (2012). A unifying model of planform straightness of ripples and dunes in air and water. *Earth-Science Reviews*, 113, 176–185. <https://doi.org/10.1016/j.earscirev.2012.03.010>
- Rubin, D. M., & Carter, C. L. (2006a). *Bedforms, and cross-bedding in animation*. SEPM Society for Sedimentary Geology. Atlas Series, 2, DVD. Retrieved from <https://cmgds.marine.usgs.gov/data/seds/bedforms/index.html>
- Rubin, D. M., & Carter, C. L. (2006b). Cross-bedding, bedforms, and paleocurrents. *SEPM concepts in sedimentology and paleontology*. Society for Sedimentary Geology. (2nd ed., Vol. 1, p. 195).
- Rubin, D. M., & Hunter, R. E. (1983). Reconstructing bedform assemblages from compound crossbedding. In M. E., Brookfield & T. S., Ahlbrandt (Eds.), *Eolian Sediments and Processes* (p. 407–427). Elsevier.
- Rubin, D. M., & Hunter, R. E. (1987). Bedform alignment in directionally varying flow. *Science*, 237(4812), 276–278. <https://doi.org/10.1126/science.237.4812.276>
- Rubin, D. M., & Ikeda, H. (1990). Flume experiments on the alignment of transverse, oblique, and longitudinal dunes in directionally varying flows. *Sedimentology*, 37(4), 673–684. <https://doi.org/10.1111/j.1365-3091.1990.tb00628.x>
- Rubin, D. M., & MacDonald, R. R. (1995). Nonperiodic eddy pulsations. *Water Resources Research*, 31(6), 1595–1605. <https://doi.org/10.1029/95wr00472>
- Rubin, D. M., Schmidt, J. C., & Moore, J. N. (1990). Origin, structure, and evolution of a reattachment bar, Colorado River, Grand Canyon, Arizona. *Journal of Sedimentary Research*, 60, 982–991.
- Shanmugam, G. (2012). Process-sedimentological challenges in distinguishing paleo-tsunami deposits. *Natural Hazards*, 63(1), 5–30. <https://doi.org/10.1007/s11069-011-9766-z>
- Sharp, R. P. (1963). Wind ripples. *The Journal of Geology*, 71(5), 617–636. <https://doi.org/10.1086/626936>
- Silvestro, S., Vaz, D. A., Ewing, R. C., Rossi, A. P., Fenton, L. K., Michaels, T. I., et al. (2013). Pervasive aeolian activity along fover Curiosity's traverse in Gale Crater, Mars. *Geology*, 41, 483–486. <https://doi.org/10.2110/60.4.540>
- Stack, K. M., Grotzinger, J. P., Lamb, M. P., Gupta, S., Rubin, D. M., Kah, L. C., et al. (2019). Evidence for plunging river plume deposits in the Pahrump Hills member of the Murray formation, Gale crater, Mars. *Sedimentology*, 66(5), 1768–1802. <https://doi.org/10.1111/sed.12558>
- Stack, M. M., Edwards, C. S., Grotzinger, J. P., Gupta, S., Sumner, D. Y., Calef, F. J., et al. (2016). Comparing orbiter and rover image-based mapping of an ancient sedimentary environment, Aeolis Palus, Gale crater, Mars. *Icarus*, 280, 3–21. <https://doi.org/10.1016/j.icarus.2016.02.024>
- Stein, N., Grotzinger, J. P., Schieber, J., Mangold, N., Hallet, B., et al. (2018). Desiccation cracks provide evidence of lake drying on Mars, Sutton Island member, Murray formation, Gale Crater. *Geology*, 46(6), 515–518. <https://doi.org/10.1130/G40005.1>
- Stein, N. T., Quinn, D. P., Grotzinger, J. P., Fedo, C., Ehlmann, B. L., Stack, K. M., et al. (2020). Regional structural orientation of the Mount Sharp group revealed by in situ dip measurements and stratigraphic correlations on the Vera Rubin ridge. *Journal of Geophysical Research: Planets*, 125(5), e2019JE006298. <https://doi.org/10.1029/2019JE006298>
- Stein, T. C., Arvidson, R. E., & Zhou, F. (2016). PDS Analyst's Notebook for MSL and MER: Addition of image measurement tools. In *47th lunar and planetary science conference*. LPI Contribution No. 1903 (p. 1192).
- Stevens, A. W., & Rubin, D. M. (2022). *Modeling surface gravity waves on a schematized ancient lake on Mars*. U.S. Geological Survey data release. <https://doi.org/10.5066/P9AA8WKP>
- Sullivan, R., Kok, J. F., Katra, I., & Yizhaq, H. (2020). A broad continuum of aeolian impact ripple morphologies on Mars is enabled by low wind dynamic pressures. *Journal of Geophysical Research: Planets*, 125, 10. <https://doi.org/10.1029/2020JE006485>
- Tanner, W. F. (1967). Ripple mark indices and their uses. *Sedimentology*, 9(2), 89–104. <https://doi.org/10.1111/j.1365-3091.1967.tb01332.x>
- Viúdez-Moreiras, D., Gómez-Elvira, J., Newman, C. E., Navarro, S., Marin, M., Torres, J., et al. (2019). Gale surface wind characterization based on the Mars Science Laboratory REMS dataset. Part II: Wind Probability Distributions. *Icarus*, 319, 645–656. <https://doi.org/10.1016/j.icarus.2018.10.010>
- Wiberg, P. L., & Harris, C. K. (1994). Ripple geometry in wave-dominated environments. *Journal of Geophysical Research*, 99(C1), 775–789. <https://doi.org/10.1029/93jc02726>
- Williams, R. M. E., Grotzinger, J. P., Dietrich, W. E., Gupta, S., Sumner, D. Y., Wiens, R. C., et al. (2013). Martian fluvial conglomerates at Gale crater. *Science*, 340(6136), 1068–1072. <https://doi.org/10.1126/science.1237317>
- Wordsworth, R. D. (2016). The climate of early Mars. *Annual Review of Earth and Planetary Sciences*, 44(1), 381–408. <https://doi.org/10.1146/annurev-earth-060115-012355>
- Yizhaq, H., Balmforth, N. J., & Provenzale, A. (2004). Blown by wind: Nonlinear dynamics of aeolian sand ripples. *Physica D:Nonlinear Phenomena*, 195(3–4), 207–228. <https://doi.org/10.1016/j.physd.2004.03.015>
- You, Z. J., & Yin, B. (2006). A unified criterion for initiation of sediment motion and inception of sheet flow under water waves. *Sedimentology*, 53(5), 1181–1190. <https://doi.org/10.1111/j.1365-3091.2006.00810.x>